Boutelier, D., Oncken, O. (2010): Role of the plate margin curvature in the plateau build-up: consequences for the Central Andes. - Journal of Geophysical Research, 115, B04402

DOI: 10.1029/2009JB006296

JOURNAL OF GEOPHYSICAL RESEARCH, VOL. 115, B04402, doi:10.1029/2009JB006296, 2010

Role of the plate margin curvature in the plateau buildup: Consequences for the central Andes

D. A. Boutelier[1] and O. Oncken[1]

Received 8 January 2009; revised 15 October 2009; accepted 9 November 2009; published 2 April 2010.

[1] The influence of convergent plate boundary curvature on the stress distribution in an overriding plate is explored using analytical and numerical modeling techniques. Trench-parallel compression can be produced near the symmetry axis of a seaward-concave plate boundary if the interplate friction is high and/or if the subducting lithosphere has a low flexural rigidity, which produces little nonhydrostatic normal stress on the plate boundary. This situation favors the formation of trench-parallel thrusts with minor trench-parallel component of slip. Trench-parallel compression is reduced along the most oblique parts of the plate boundary, which favors the formation of strike slip faults with major trench-parallel slip. Both the stress conditions on the interplate zone and the 3-D geometry of this zone control whether the trench-parallel stress in the center of a seaward-concave curvature is a tension or compression. Low dip angle and high convergence obliquity angle favor trench-parallel compression. In the central Andes, N-S minor shortening in the center of the Arica bend and strike slip systems north and south of the symmetry axis suggest that the effect of shear traction dominated during Cenozoic time when the curvature of the plate boundary was forming. This result suggests that the processes responsible for the formation of the plate boundary curvature were assisted by enhanced interplate friction and/or reduced compressive nonhydrostatic normal stress. For a geometry resembling the present-day South American plate margin, estimations of normal and shear stresses on the plate boundary suggest that the trench-parallel stress in the center of the curvature is compressive.

Citation: Boutelier, D. A., and O. Oncken (2010), Role of the plate margin curvature in the plateau buildup: Consequences for the central Andes, *J. Geophys. Res.*, *115*, B04402, doi:10.1029/2009JB006296.

1. Introduction

[2] A number of active convergent continental plate boundaries have experienced long-lived shortening resulting in the formation of fold-and-thrust belts. The eastern margin of the Pacific Ocean constitutes the best example with the North and South American cordilleras extending over several thousands of kilometers along plate boundaries [*Dickinson*, 2004; *Hyndman et al.*, 2005; *Franz et al.*, 2006]. However, within these zones, the central Andes are significantly different because the fold-and-thrust belt evolved into a plateau belt in Cenozoic time [*Allmendinger et al.*, 1997; *Oncken et al.*, 2006]. The Altiplano-Puna plateau in the central Andes (Figure 1) reaches a high average elevation of ~4000 m resulting from important crustal thickening combined with lithospheric thinning through thermal erosion and/or delamination/convective removal of the mantle root [*Isacks*, 1988; *Kay and Kay*, 1993; *Beck and Zandt*, 2002]. Crustal thickening is mostly due to the generally east-west tectonic shortening of the South American western margin and magmatic underplating [*Isacks*, 1988; *Allmendinger et al.*, 1997; *Haschke and Günther*, 2003; *Hindle et al.*, 2005].

[3] The buildup of the Altiplano-Puna plateau in the central Andes has required more intense shortening of the continental crust near the oroclinal bend than elsewhere along the plate boundary. The total horizontal E-W crustal shortening is estimated to be ~300 km in the center of the plateau (i.e., at 19°S) but only ~140–160 km at the northern and southern edges of the plateau [*Kley and Monaldi*, 1998; *Oncken et al.*, 2006]. This observation suggests a focusing of the plate-boundary push along the Andean margin between 10 and 33°S. A number of mechanisms have been suggested to be responsible for this pattern. They include latitudinal variations of the initial and boundary conditions, such as the variations of push on the plate boundary [*Molnar and Atwater*, 1978; *Jordan et al.*, 1983] or a preexisting structural segmentation of the margin [*Kley and Monaldi*, 1998; *Kley et al.*, 1999]. Similarly, spatial and temporal climate variations have also been proposed as possible mechanisms [*Raymo and Ruddiman*, 1992; *Horton*, 1999; *Montgomery et al.*, 2001; *Hartley*, 2003; *Lamb and Davis*, 2003]. However, most of these mechanisms take a 2-D perspective. They

---

[1] Helmholtz-Zentrum Potsdam Deutsches GeoForschungsZentrum, Potsdam, Germany.

0148-0227/10/2009JB006296

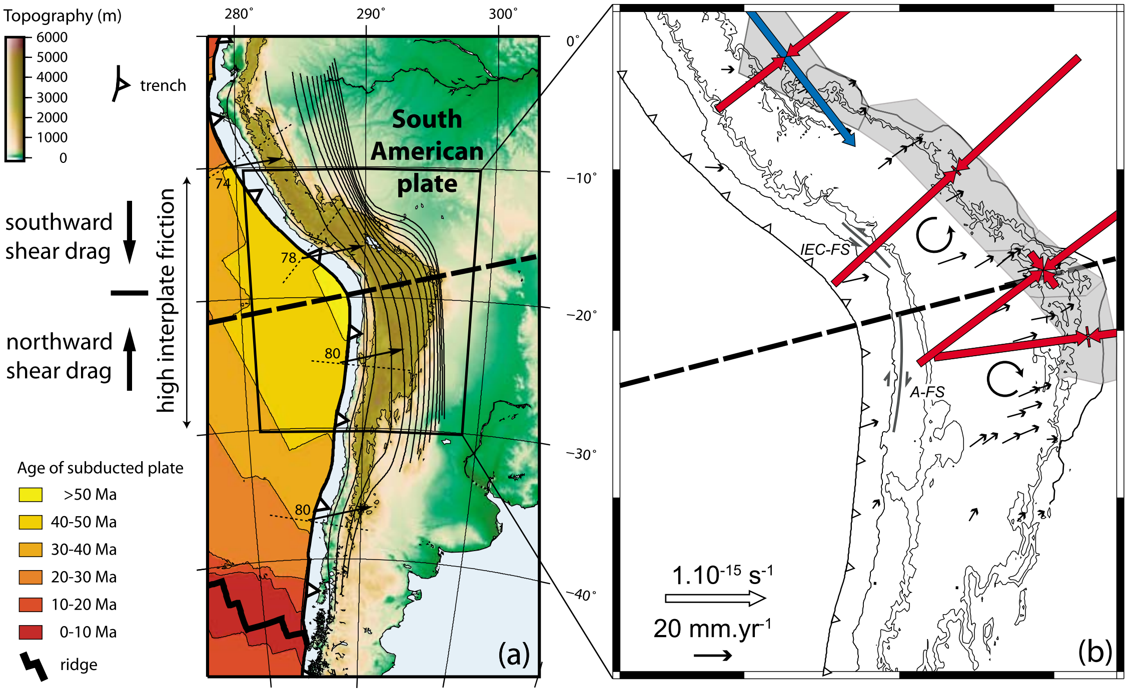

Figure 1. (a) Map of the South American plate margin between 0 and 50°S showing the curvature of the plate margin at 20°S and the topography of the Andes. The vectors along the plate margin represent the NUVEL1A convergence velocity between the Nazca and South American plates [*DeMets et al.*, 1994] (velocity in mm yr^{-1}). The direction perpendicular to the trench is plotted with thin dotted lines to highlight the obliquity of the convergence. The heavy dashed line represents the line with zero plate convergence obliquity. It also roughly corresponds to the present-day symmetry axis of the orogen [*Gephart*, 1994]. Thin solid lines represents the slab isodepths from *Gudmundsson and Sambridge* [1998] (contours every 50 km). (b) Zoom-in on the central Andes with the kinematic model by *Kley* [1999] and the geological strain rates by *Hindle et al.* [2002] showing trench-parallel shortening in the vicinity of the symmetry axis in the Eastern Cordillera. South of the symmetry line, paleomagnetic rotations are generally clockwise, while north of this line paleomagnetic rotations are generally counterclockwise. Right-lateral sense of displacement is observed in trench-parallel faults in the fore arc south of the symmetry line (A-FS, Atacama fault system), while left-lateral sense of motion is observed north of the line (IEC-FS, Incapuquio-El Castillo fault system).

rarely take into account the observation that the plateaus of the central Andes are located near the bend of the orogen marked by a symmetry axis [*Gephart*, 1994] (Figure 1). *Russo and Silver* [1994, 1996] and *Schellart et al.* [2007] have proposed 3-D models of the formation of the orocline due to the large-scale interaction between the subducted slab and the upper mantle. In these studies the curvature of the plate boundary is a result of the model. We investigate the idea that this seaward-concave curvature also participates in generating more shortening in the central Andes and is therefore an additional driving factor of the plateau buildup. Crustal volume balancing has revealed that the shortening mechanism is fundamentally three-dimensional [*Hindle et al.*, 2005], and the position of the plateau near the symmetry axis of the plate boundary is not fortuitous but is a fundamental characteristic of the orocline bending process.

[4] Because of the in-plane curvature of the trench, the convergence between the Nazca and South American plates is oblique both north and south of a line of zero-obliquity that corresponds approximately to the symmetry axis of the present-day plate boundary (Figure 1). Oblique plate convergence produces a trench-parallel shear drag on the fore arc [*Fitch*, 1972; *McCaffrey*, 1991, 1992, 1996; *Chemenda et al.*, 2000]. For relatively high values of the obliquity angle, the convergence can be partitioned between a less oblique slip on the plate boundary and a trench-parallel displacement of a fore-arc sliver [*Jarrard*, 1986a, 1986b; *McCaffrey*, 1991, 1992]. Consequently, to accommodate the fore-arc lateral motion, the overriding plate margin undergoes trench-parallel extension or shortening [*Ave Lallemant*, 1996; *McCaffrey and Nabalek*, 1998]. In the case of the central Andes, the obliquity changes sign across the symmetry line. Therefore north of this line the arc/fore arc is dragged southward while south of the line it is dragged northward (Figure 1). In other words, material is being pulled toward the axis of the bend from the oblique sections of the orogen, north and south of the axis. This lateral traction may be the cause of the north-south shortening of the fore-arc and back-arc domains near the symmetry line. In the fore arc, the N-S shortening is evidenced by a suite of E-W pure dip slip thrusts in the Coastal Cordillera between 19 and 21.6°S [*Allmendinger et al.*, 2005]. Further inland the N-S shortening is documented in kinematic models

[*Dewey and Lamb*, 1992; *Kley*, 1999; *Arriagada et al.*, 2008]. The displacement field, derived from paleomagnetic data, shortening estimates from balanced cross sections, and variations of crustal cross-sectional area, suggests that material from the Eastern Cordillera, Interandean zone and Subandean belt has moved toward the bend [*Kley*, 1999; *Arriagada et al.*, 2008]. The bulk strain rates computed from the kinematic model by *Kley* [1999] reflect this observation [*Hindle et al.*, 2002]: geological rates derived from data averaged over the last 10 or 25 Ma both reveal a slow (1×10^{-16} s^{-1}) orogen parallel (N-S) shortening in the Eastern Cordillera near the bend (Figure 1b). Despite being minor compared to the orogen-perpendicular shortening ($1 \times 10^{-15} s^{-1}$), this N-S shortening is significant since it allows crustal volume balancing [*Hindle et al.*, 2005] and provides a constraint on the mechanism responsible for the bending of the orocline and buildup of the plateaus that we investigate in this study. The hypothesis that the N-S shortening included in the kinematic models is due to the horizontal drag of the fore arc toward the bend is further supported by paleomagnetic studies showing Cenozoic clockwise block rotations south of the bend and anticlockwise block rotations north of it [*Beck*, 1998; *Roperch et al.*, 1999, 2000; *Lamb*, 2001; *Rousse et al.*, 2003, 2005].

[5] This portrait is however the opposite of that actually obtained from numerical computations where the nonhydrostatic normal stress generated by subduction is imposed on a seaward-concave interplate zone [*Boutelier*, 2004]. Trench-parallel tension is then observed near the symmetry axis in the overriding plate instead of the compression that one would expect in order to produce the N-S shortening. A similar result is also obtained when the subduction process is fully modeled in 3-D, and both the nonhydrostatic normal stress and shear stress due to oceanic subduction are imposed on a seaward-concave interplate zone [*Bonnardot et al.*, 2008]. The reason may be that the lateral drag of the fore arc is due to the shear traction on the plate boundary, but this effect may be overcome by the action of the nonhydrostatic normal stress on the interface. The latter is perpendicular to the oblique segments of the plate boundary and therefore produces diverging compressive stress trajectories in the overriding plate. This divergence results in a trench-parallel tension and dynamic subsidence in the overriding plate near the curvature symmetry axis [*Boutelier*, 2004; *Bonnardot et al.*, 2008]. These results suggest that either the trench-parallel shortening observed in the central Andes is not an effect of the plate boundary geometry but is generated by another unknown process, or the stress conditions along the interplate zone and/or the geometry of this zone allowed the effects of the nonhydrostatic normal stress to be counterbalanced. This latter interpretation leads to an important question: Under which conditions can the seaward-concave geometry of the plate boundary produce a trench-parallel (N-S) shortening near the symmetry line of the bend?

[6] Using a combination of analytical and numerical methods, we investigate the role of the interplate dip angle, the plate convergence obliquity angle, and the level of interplate coupling in producing trench/orogen-parallel compression. We show that the location of such trench/orogen-parallel compression in the center of a seaward-concave bend of the plate boundary can be reconciled with the effects of subduction-induced stresses on curved convergent plate boundaries. In order to produce larger trench-parallel compression near the symmetry line of the curvature than elsewhere along the plate margin, the level of interplate coupling must be high, the dip angle of the interplate zone must be low, and the plate convergence obliquity should be relatively important.

2. Analytical and Numerical Approach

2.1. Stress Boundary Conditions

[7] During oceanic subduction, the interface between the subducting and overriding plates is submitted to a nonhydrostatic normal stress and a shear stress. Horizontal tectonic stresses are then generated inside the overriding plate, producing back-arc opening/spreading when the tectonic stress in the convergence direction is tensile, or arc/back arc shortening with formation of a fold-and-thrust belt or subduction of the fore-arc/arc plate if the tectonic stress in the convergence direction is compressive.

[8] The total force applied on the interplate zone can be written as

$$F_p = \int_S P_h dS + \int_S \sigma_n dS + \int_S \tau dS \tag{1}$$

where P_h is the hydrostatic pressure, σ_n is the nonhydrostatic normal stress, and τ is the shear traction on the interface between the plates S. Because τ is believed to be small for subduction zones [*Tichelaar and Ruff*, 1993; *Peacock*, 1996; *Hassani et al.*, 1997], the integration of σ_n over the surface area S produces the main tectonic force acting on this zone, F_n. The nonhydrostatic normal stress is caused by the flexural rigidity of the subducting lithosphere, the slab pull force, and the viscous force due to the interaction with the asthenosphere [*Shemenda*, 1993; *Scholz and Campos*, 1995; *Royden and Husson*, 2006; *Boutelier and Cruden*, 2008]. Assuming that the interplate zone has a dip angle α constant with depth, the force F_n resulting from the application of the depth-averaged nonhydrostatic normal stress $\overline{\sigma}$ is perpendicular to this zone and can be decomposed into horizontal and vertical components, the magnitudes of which depend on the dip angle (Figure 2a). In the case of compressive oceanic subduction, the horizontal component of the force F_n is oriented toward the interior of the overriding plate and is locally perpendicular to the direction of the trench, while the vertical component drives the fore-arc area upward. The variation of the components of F_n with α is then simply given by

$$(F_n)_h = \bar{\sigma} \times S \times \sin(\alpha) \tag{2}$$

$$(F_n)_v = \bar{\sigma} \times S \times \cos(\alpha) \tag{3}$$

[9] The upward vertical component $(F_n)_v$ generates a positive gravity anomaly in the fore-arc area [*Shemenda*, 1993]. Computation of the free-air gravity anomalies derived from deformed numerical models [*Tang and Chemenda*, 2000; *Tang et al.*, 2002] allowed the estimation of the magnitude of the depth-averaged nonhydrostatic

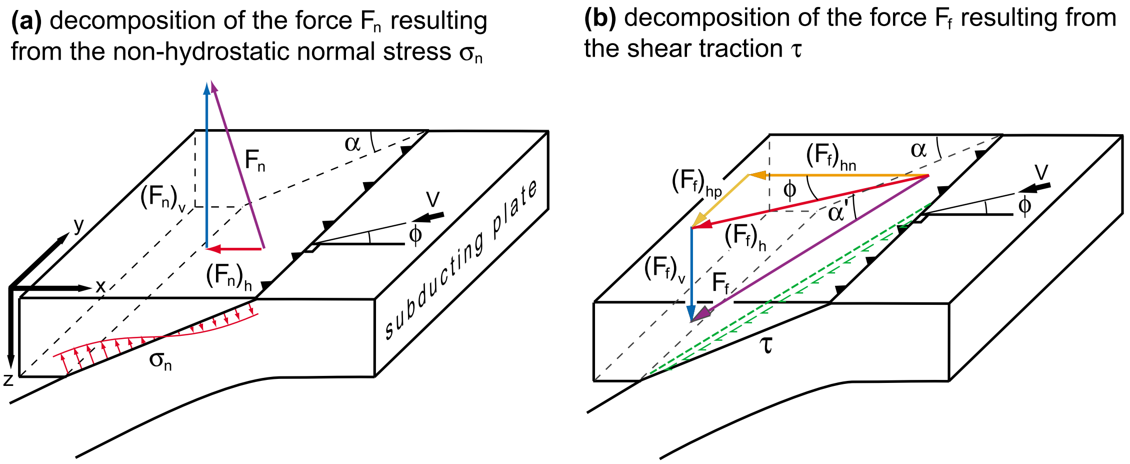
(a) decomposition of the force F_n resulting from the non-hydrostatic normal stress σ_n

(b) decomposition of the force F_f resulting from the shear traction τ

Figure 2. Sketches of the decomposition of (a) the force F_n due to the nonhydrostatic normal stress and (b) the force F_f generated by the shear traction acting on the interface between the plates. $(F_n)_v$ and $(F_n)_h$ are the vertical and horizontal components of the force F_n; σ_n is the nonhydrostatic normal stress on the plate boundary, whose magnitude and sense vary with depth [*Shemenda*, 1993; *Tang et al.*, 2000]; ϕ is the obliquity of the plate convergence represented by the vector V; α is the true dip of the plate boundary (assumed to be constant with depth for simplicity); α' is the apparent dip, the dip of the plate boundary in the horizontal direction of the convergence; τ is the shear traction on the plate boundary. Integration of τ on the surface area of the interplate zone gives the force F_f whose horizontal and vertical components are $(F_f)_h$ and $(F_f)_v$, respectively. The horizontal component $(F_f)_h$ is composed of a trench-parallel component $(F_f)_{hp}$ and a trench-normal component $(F_f)_{hn}$.

normal stress on the interplate zone. The magnitudes of the gravity anomalies in the trench and the fore arc in a compressive subduction zone are reproduced with a depth-averaged nonhydrostatic normal stress of ~100 MPa [*Tang and Chemenda*, 2000; *Tang et al.*, 2002]. For tensile subduction zones, the depth-averaged nonhydrostatic normal stress becomes negative (i.e., trench suction) but its magnitude remains uncertain [*Shemenda*, 1993].

[10] The interplate zone is generally lubricated by subducted fluids and/or sediments, and the mean shear stress is estimated to be small, on the order of ~15 MPa [*Tichelaar and Ruff*, 1993; *Peacock*, 1996; *Lamb*, 2006]. However, if the interface between the plates is poorly lubricated, the friction coefficient may increase significantly, and the mean shear stress is estimated to be in the range ~40–100 MPa [*Molnar and England*, 1990; *Lamb and Davis*, 2003; *Husson and Ricard*, 2004; *Lamb*, 2006]. The force F_f resulting from the application of the depth-averaged shear traction can also be decomposed into vertical and horizontal components (Figure 2b). The vertical component of this force drives the fore arc downward. Because the horizontal component $(F_f)_h$ is parallel to the direction of the plate convergence, we further decompose it into a trench-normal component $(F_f)_{hn}$, similar to the horizontal component $(F_n)_h$ of the force due to the nonhydrostatic normal stress, and a trench-parallel component $(F_f)_{hp}$ (Figure 2b). Finally, the components of the force generated by the shear stress also depend on the convergence obliquity angle ϕ. With higher obliquity, the apparent dip angle α' of the interplate zone decreases, and consequently, $(F_f)_{hp}$ increases, while $(F_f)_{hn}$ decreases:

$$\alpha' = \arctan(\cos(\phi) \times \tan(\alpha)) \tag{4}$$

$$(F_f)_{hn} = \overline{\tau} \times S \times \cos(\alpha') \times \cos(\phi) \tag{5}$$

$$(F_f)_{hp} = \overline{\tau} \times S \times \cos(\alpha') \times \sin(\phi) \tag{6}$$

[11] We used the decomposition of the forces due to the nonhydrostatic normal stress and shear stress to compute the magnitude of the normal and tangential stresses imposed in a 2-D numerical model in order to investigate the generated horizontal stress field in the overriding plate. The plate boundary is composed of multiple segments, each characterized by a dip angle α, convergence obliquity angle ϕ, and the level of coupling on the interface between the plates ($\overline{\sigma}$ and $\overline{\tau}$). The horizontal force components are computed for each individual segment whose length is normalized. The trench-parallel force component $(F_f)_{hp}$ is imposed via an oriented tangential stress applied on the segment, while the sum of the trench-normal force components, $(F_n)_h + (F_f)_{hn}$, is imposed via a normal stress.

2.2. Setup of Numerical Modeling

[12] Using the finite element code ADELI [*Hassani et al.*, 1997], we compute the horizontal stress field in an overriding lithosphere submitted to various stress conditions along the interplate zone. The model lithospheric plate is reduced to a 2-D horizontal plane with dimensions 1500 × 3000 km (Figure 3). Vertically averaged stresses are applied to the interplate zone, which corresponds to the western edge of the plate in the 2-D plan view. The model plate possesses a simple elastic rheology with a Young modulus of 10^{11} Pa and a Poisson coefficient of 0.25 since we do not compute the large deformation. A free-slip boundary con-

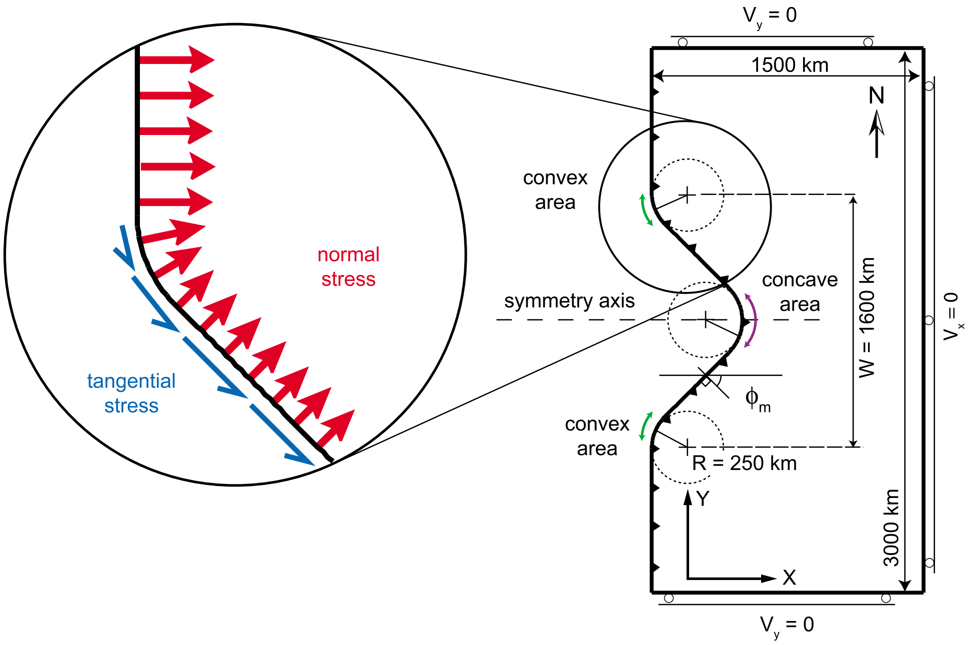

Figure 3. Schematic representation of the numerical model setup. The plate is modeled in the horizontal plane (no thickness). The model plate boundary contains two seaward-convex areas, one seaward-concave area, and two segments of constant maximum obliquity ϕ_m. The stresses (normal and tangential) applied on the plate boundary vary along the strike with the convergence obliquity. W is the width of the oblique part of the plate boundary, and R is the curvature radius of the convex and concave areas.

dition is applied to the three remaining edges of the model plate (northern, southern, and eastern edges). This setup represents the case where subduction is toward the east and convergence direction is perfectly E-W. The plate boundary is curved, and therefore the convergence obliquity angle varies along the strike of the trench. We used the decomposition of the forces presented above to compute the normal and tangential stresses on the plate boundary (in plan view) depending on the assumed global value of α, $\overline{\sigma}$ and $\overline{\tau}$ (i.e., assumed to be true for the whole length of the plate boundary) and the local value of ϕ. The seaward-concave curved area near the symmetry axis of the model and the two seaward-convex curved areas (north and south of the model symmetry axis) have the same curvature radius of 250 km (Figure 3). In between the curved areas the obliquity angle is constant (45°, 20°, or 10°). These geometries do not represent the Andean plate boundary as we aim at understanding the effects of the parameters in a simplified and symmetrical system.

[13] The employed technique allows the computation of the horizontal stress field generated by the application of the horizontal components of the forces acting on the plate boundary. However, the passage from 3-D to 2-D using depth-averaged parameters on the plate boundary prevents us from modeling the stress field in the fore-arc area because this zone is collapsed into the edge of the 2-D model.

[14] The interplate dip angle, the averaged nonhydrostatic normal stress and shear traction are assumed to be constant along the strike of the plate boundary. This simplification allows differentiating the effect of the plate boundary geometry from that of the lateral variations of these parameters, which can occur independently [*Molnar and Atwater*, 1978; *Jordan et al.*, 1983; *Kley et al.*, 1999]. Shear traction can change dramatically along strike because of the presence or absence of sediment input in the trench due to the variations in local climate. Subducting ridges can also inhibit sediment flux in the trench, and therefore the lateral or trench-parallel variations in the level of coupling can certainly be sharp. The nonhydrostatic normal stress depends on the flexural rigidity of the subducting lithosphere, the slab pull force, and the flow in the asthenosphere which are not expected to vary significantly on short spatial scales, except, however, for the subduction of oceanic ridges and plateaus and the existence of tears in the subducting lithosphere. Subduction of ridges and plateaus is a well-acknowledged feature of the subduction history along the South American plate margin [*Jordan et al.*, 1983]. We voluntarily ignore these spatial variations in order to focus on the effect of the plate boundary geometry.

[15] For each stress boundary condition applied on the subduction zone, we computed the orientations and magnitudes of the main stresses and the distributions of J_2, the second invariant of the deviatoric stress tensor. J_2 is a scalar function of the principal deviatoric stress tensor components, which remains identical regardless of the coordinate system and quantifies the shear stress.

3. Results

3.1. Run 1: Influence of the Nonhydrostatic Normal Stress

[16] In run 1 (Figures 4a–4c) a normal stress of 10 MPa is imposed on the plate boundary. This corresponds to the horizontal component of the force generated by the application of a 10 MPa non-hydrostatic normal stress [*Tang and*

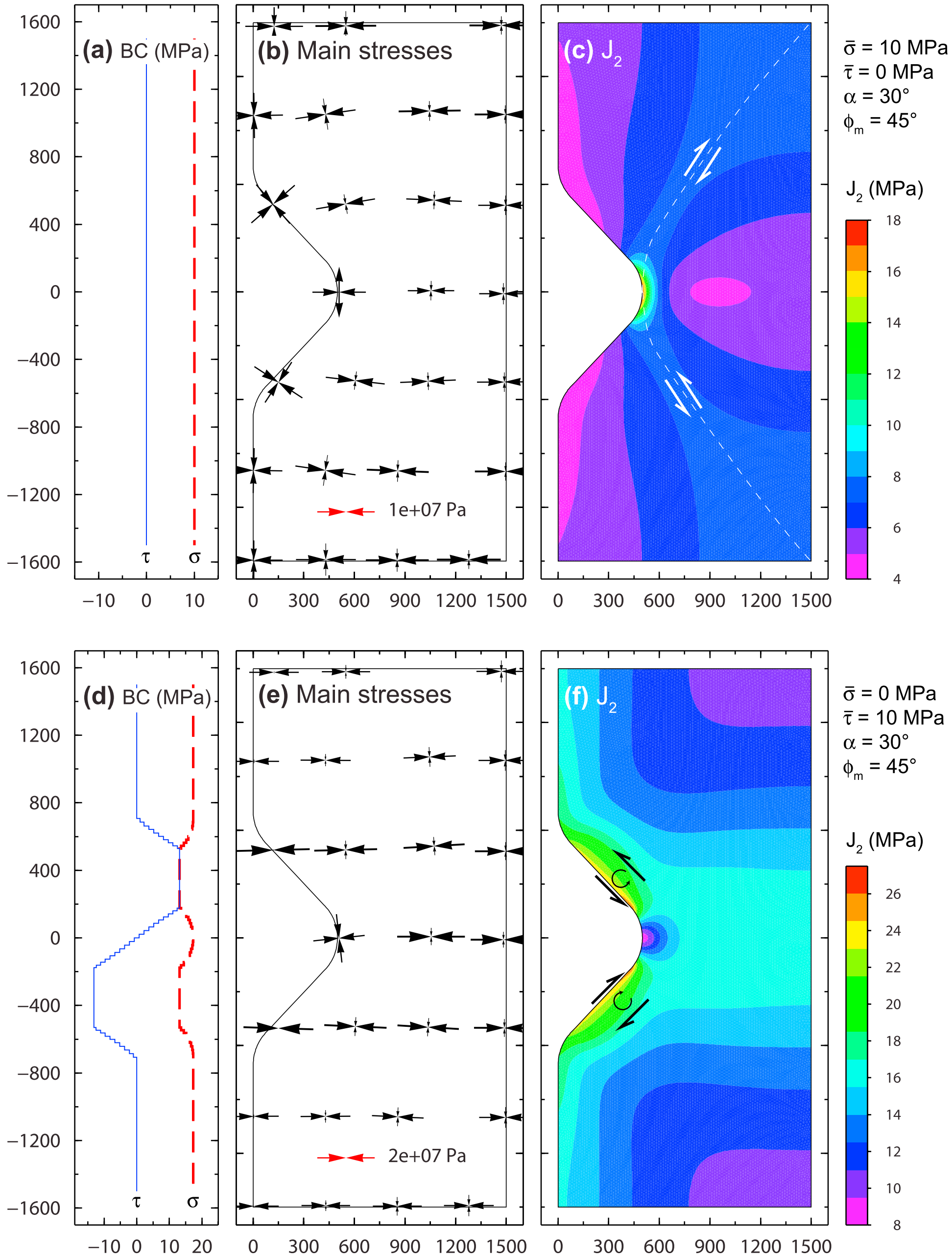

Figure 4. Experimental results for runs 1 and 2. In run 1 (Figures 4a–4c), a normal stress due to the horizontal component of the force F_n is applied to the plate boundary, while there is no shear traction (perfectly lubricated subduction zone). (a) The boundary conditions do not depend on the obliquity of the convergence. The dashed line represents the normal stress, while the solid line represents the tangential stress (positive in the trigonometric sense). (b) Main stresses. (c) Second invariant of the deviatoric stress tensor J_2 (pattern1). In run 2 (Figures 4d–4f), normal and tangential stresses due to the horizontal components of the force F_f are imposed on the plate boundary. (d) The boundary conditions change along strike because of the variations of ϕ. (e) Main stresses in run 2. (f) Second invariant of the deviatoric stress tensor J_2 (pattern 2). The black arrows show the strike-slip sense of shear in areas of high horizontal shear stress (high values of J_2). See text for details.

Chemenda, 2000; *Tang et al.*, 2002] on a plate boundary inclined at 30° (Figure 4a). The plate boundary is assumed to be perfectly lubricated, and the shear traction is zero. Near the plate boundary, the most compressive horizontal stress σ_{Hmax} is perpendicular to this zone (Figure 4b), while the least compressive stress σ_{Hmin} is parallel to it. The latter changes sign along the margin (Figure 4b). Near the intersection of the plate boundary and symmetry axis, σ_{Hmin} is oriented N-S and is tensile. Elsewhere along the margin, σ_{Hmin} is parallel to the trench, and compressive (Figure 4b). The second invariant of the deviatoric stress tensor J_2 also reflects this spatial distribution: it is maximal near the intersection of the trench and symmetry axis of the curvature, and two branches of higher values of J_2 (i.e., higher horizontal shear stress) start from this location and join the NE and SE corners of the model plate (we hereafter refer to this distribution as pattern 1, Figure 4c). The relative values of the horizontal stresses allow us to predict the style of deformation in specific parts of the model. In this run, we obtained a N-S horizontal tension in the center of the seaward-concave curvature of 10.5 MPa together with a strong E-W compression of 9.7 MPa (Figure 4b). In this area, σ_{Hmax} naturally corresponds to the most compressive stress σ_1. Because σ_{Hmin} is tensile we can also conclude that it corresponds to the least compressive stress σ_3. This situation does not favor the buildup of thrusts and vertical thickening in this area but rather the development of strike-slip faults (i.e., the branches of higher values of J_2), allowing the horizontal extrusion of the plate. In the most oblique sections of the plate boundary, σ_{Hmin} is highly compressive (~ 8.9 MPa) and thus may correspond to the intermediate main stress σ_2 rather than σ_3.

3.2. Run 2: Influence of the Shear Traction

[17] In run 2 (Figures 4d–4f) the normal and tangential stresses corresponding to the horizontal components of the force F_f are applied on the plate boundary (Figure 4d). These components are computed analytically using $\overline{\tau}$ = 10 MPa, α = 30° and the local value of ϕ along the trench. The most compressive horizontal stress σ_{Hmax} is generally oriented E-W while the least compressive horizontal stress σ_{Hmin} is oriented N-S. The latter is significantly smaller than σ_{Hmax} except near the intersection of the plate boundary and symmetry axis of the curvature where $\sigma_{\mathrm{Hmin}} \sim \sigma_{\mathrm{Hmax}}$ (17 and 18 MPa, respectively). Along the most oblique segments of the plate boundary and near the two seaward-convex areas, σ_{Hmin} reduces to zero and becomes tensile near the seaward-convex areas (0.5 MPa). The second invariant of the deviatoric stress tensor J_2 is now minimal near the intersection of the trench and symmetry axis of the model plate and maximal along the two most oblique sections of the plate boundary (we hereafter refer to this distribution as pattern 2: see Figure 4f). Near the intersection of the plate boundary and symmetry axis, the most compressive horizontal stress σ_{Hmax} must be σ_1, and the least compressive horizontal stress σ_{Hmin} could be σ_2 if the vertical stress is small or σ_3 if the vertical stress is already large because, for example, of intense thickening. However, since the least compressive horizontal stress is almost as compressive as the most compressive stress, we can safely assume that the former corresponds to the intermediate principal stress σ_2, and that therefore σ_3 is vertical. This situation favors the development of thrust faults and thus thickening in the center of the seaward-concave curved area as in the central Andes. The second invariant of the deviatoric stress tensor is maximal along the most oblique sections of the plate boundary (Figure 4f), which suggests the development of strike-slip systems locally parallel and close to the plate boundary and less vertical thickening, a picture also resembling the Andes (Figure 1).

3.3. Variations of Interplate Coupling

[18] In nature, both forces generated by the nonhydrostatic normal stress and shear traction are acting on the plate boundary. It is rather obvious that in order to obtain a stress pattern similar to that generated in run 2, the amount of shear stress on the plate boundary should be increased with respect to the nonhydrostatic normal stress. We define Ω as the ratio of the depth-averaged shear traction over the depth-averaged nonhydrostatic normal stress ($\Omega = \overline{\tau}/\overline{\sigma}$). For the employed geometry of the plate boundary (φ_{m} = 45° and α = 30°), the transition between the patterns 1 and 2 occurs for the threshold value Ω_{l} = 0.6 to 0.7. As Ω becomes closer to Ω_{l}, the lobe of high values of J_2 splits into two lobes that progressively migrate toward the most oblique sides of the plate boundary (Figure 5). Correspondingly, the N-S main stress in the center of the seaward-convex curvature changes from a tension of 8.6 MPa for Ω = 0.4 (Figure 5a) to a compression of 2.5 MPa for Ω = 0.7 (Figure 5b) and 7 MPa for Ω = 1.0 (Figure 5c), while the E-W main stress always remains highly compressive (27 to 42 MPa).

3.4. Variations of Interplate Geometry

[19] The ratio Ω represents the balance of the nonhydrostatic forces acting on the plate boundary. This parameter clearly influences the stress distribution in the overriding plate. However, for one value of Ω, the geometry of the plate margin will also influence the distribution of the force components (see equations (2) to (6)) and thus the stress distribution inside the plate. Both angles α and ϕ affect the produced stress distribution because the interplate zone is a three-dimensional object.

3.4.1. Interplate Zone Dip Angle

[20] Figure 6 shows the variations of the distribution of J_2 associated with the variations of α. Small dip angles generate larger surface areas of the interplate zone which allow transmitting larger forces to the upper plate. This variation of the surface area, however, does not change the distribution of force components. In that matter the surface orientation is more important because small dip angles also promote larger horizontal components of shearing force F_f and smaller horizontal component of the nonhydrostatic pressure force F_n. This tends to produce the second pattern (Figure 6a), and a larger N-S compression in the center of the seaward-concave curvature. In Figure 6, the imposed depth-averaged shear traction and nonhydrostatic normal stress are 5 and 10 MPa, respectively (Ω = 0.5). For α = 30°, this stress conditions produce a N-S tension of 2 MPa in the center of the seaward-concave curvature, which becomes a compression of 3 and 5 MPa for α = 20 and 10°, respectively. The E-W stress in this area, however, always remains highly compressive (38, 23 and 18 MPa for α = 10, 20, and 30°, respectively). For any value of α, there is a threshold value of Ω for which the transition between the two patterns

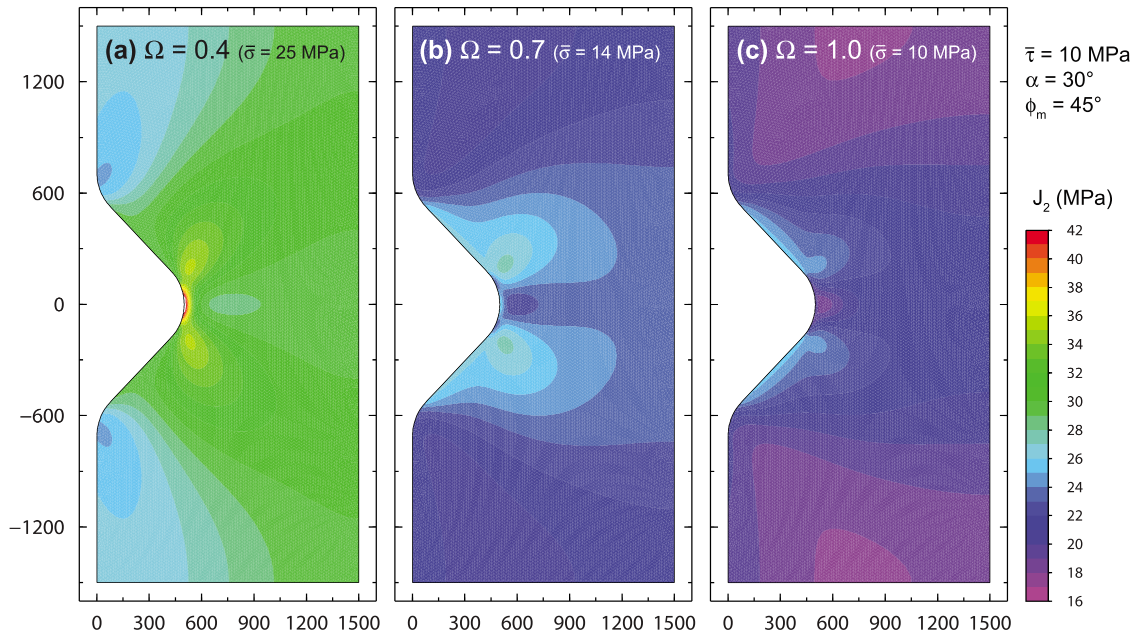

Figure 5. Variations of the distribution of the second invariant of the deviatoric stress tensor J_2 with variations of the ratio Ω of the shear traction $\overline{\tau}$ over the nonhydrostatic normal stress $\overline{\sigma}$. In the three runs, the geometry of the plate boundary is constant with a maximum convergence obliquity angle ϕ_m of 45° and a dip angle α of 30°. In the three runs, the depth-averaged shear traction $\overline{\tau}$ is 10 MPa. (a) The depth-averaged nonhydrostatic normal stress $\overline{\sigma}$ is 25 MPa ($\Omega = 0.4$); (b) $\overline{\sigma}$ is 14 MPa ($\Omega = 0.7$); (c) $\overline{\sigma}$ is 10 MPa ($\Omega = 1$). For low values of Ω, the pattern of J_2 is similar to that obtained in run 1 (generated by $\overline{\sigma}$) with the maximum located in the center of the curvature (see Figure 4c). For high values of Ω, the pattern becomes similar to that obtained in run 2 (generated by $\overline{\tau}$) with the maximum of J_2 located along the most oblique parts of the plate boundary (see Figure 4f). A transition between the two patterns occurs for this geometry ($\phi_m = 45°$ and $\alpha = 30°$) for $\Omega_l = 0.6$ to 0.7 (Figure 5b).

occurs. We investigated the variations of the threshold value Ω_l when varying the dip angle. With a maximum convergence obliquity angle of 45° and a dip angle of 30°, Ω_l is 0.6–0.7. However, when α is only 20° (as in central Chile [*Cahill and Isacks*, 1992]), Ω_l decreases to 0.4–0.5 and further drops to 0.2 when α is 10°. The less inclined the plate boundary, the less shear traction is required to counterbalance the effect of the nonhydrostatic normal stress.

3.4.2. Interplate Zone in-Plane Curvature

[21] The in-plane curvature of the plate boundary also contributes to the stress distribution pattern. Increasing the maximum obliquity angle ϕ_m along the sides of the curved area locally produces a larger trench-parallel horizontal component of the force F_f (equations (5) and (6)) and thus regionally promotes pattern 2. We tested the variations of Ω_l when varying the maximum obliquity angle ϕ_m without changing the width of the curved area W or the curvature radii (see Figure 3). As mentioned above, for a maximum obliquity angle ϕ_m of 45° and a dip angle α of 20°, the threshold value between the two patterns is 0.4–0.5. For a maximum obliquity angle ϕ_m of only 20° the threshold value increases to 0.6, and further increases to 0.7 for $\phi_m = 10°$. The variation of J_2 also becomes smaller with smaller maximum convergence obliquity angle (Figure 7). However, with the imposed stresses and employed geometry presented in Figure 7c, the N-S stress in the center of the seaward-concave curvature is reduced by a significant ~10% compared to the N-S away from the curvature. The less oblique the plate boundary, the more shear traction is required to counterbalance the effect of the nonhydrostatic normal stress, and even for a very low maximum obliquity angle, it is possible to produce the largest N-S compression in the center of the seaward-concave curved area if $\overline{\tau} > \Omega_l \times \overline{\sigma}$.

4. Discussion

4.1. Comparison of the Two Model Types With Geological Data

[22] The South American plate boundary has been classically presented as the typical example of a compressive oceanic subduction zone because of the observation of intense shortening of the arc/back-arc area [*Uyeda and Kanamori*, 1979]. This compressive oceanic subduction regime can be produced in analog and numerical modeling experiments when the subducting oceanic lithosphere is not significantly denser than the surrounding mantle [*Shemenda*, 1993; *Hassani et al.*, 1997]. In that case, the flexural rigidity of the downgoing plate produces a compressive nonhydrostatic normal stress on the interplate zone, which generates a trench-normal compressive horizontal stress in the overriding plate. The horizontal compression can also be obtained in 2-D simulations by a combination of both nonhydrostatic normal stress and high interplate friction [*Hassani et al.*, 1997; *Sobolev and Babeyko*, 2005; *Sobolev et al.*, 2006]. However, in nature the shortening of the arc/back arc in the

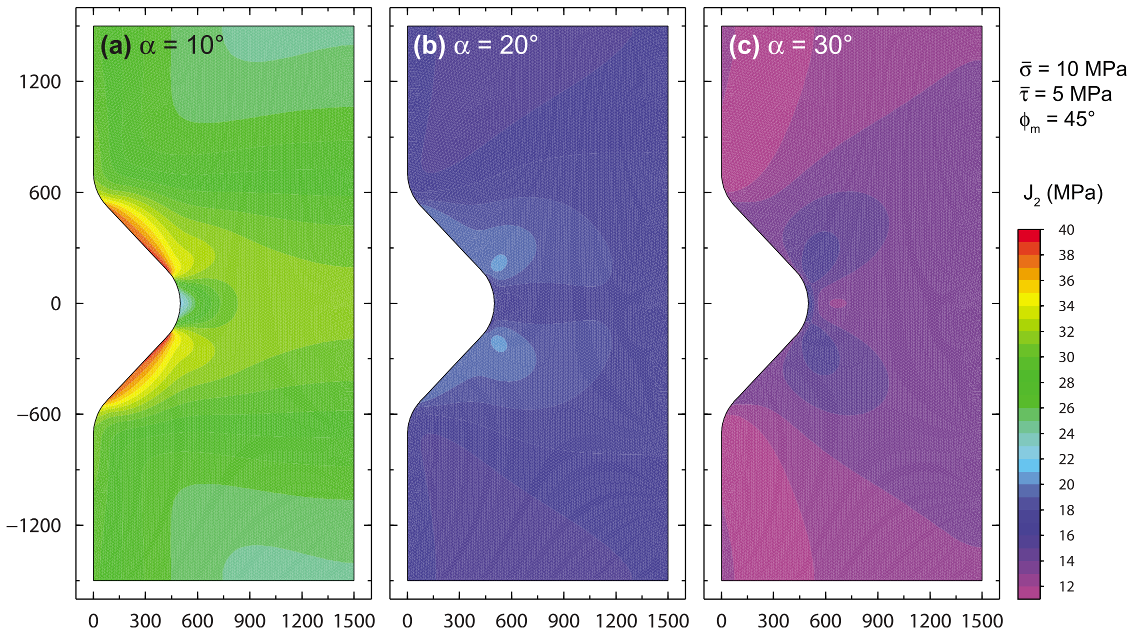

Figure 6. Variations of the distribution of the second invariant of the deviatoric stress tensor J_2 with variation of the dip angle α. Ω is constant in these runs at 0.5 ($\overline{\sigma}$ = 10 MPa, and $\overline{\tau}$ = 5 MPa), and the maximum convergence obliquity angle ϕ_m is constant at 45°. (a) For low values of the dip angle α, the applied stresses produce the pattern of J_2 obtained in run 2 (generated by $\overline{\tau}$). (c) For high values of the dip angle, the pattern of J_2 becomes similar to that obtained in run 1 (generated by $\overline{\sigma}$). (b) A transition between the two patterns is obtained for this curvature angle and stress conditions with α = 20.

central Andes is three-dimensional, and the observation of N-S shortening in the center of the seaward-concave curvature and significant horizontal component of slip along the most oblique parts of the plate boundary suggest that the shear traction along the interplate zone plays an important role in the shortening mechanism. What can this N-S shortening tell us about the mechanisms of orocline bending and plateau buildup? To answer this question, we investigated the effects of several key parameters thought to control the distribution of tectonic stresses in the overriding plate. We obtained two main stress fields (associated with the pattern 1 and 2 of J_2) which can be compared with geological data in the Andes.

[23] Imposed along a seaward-concave plate boundary, the nonhydrostatic normal stress produces a trench-parallel tension near the intersection of the curvature axis and plate margin (Figures 4a–4d). In our experiments, this tension extends hundreds of kilometers away from the point of application of the boundary conditions toward the interior of the plate. However, this point of application represents the whole width of the interplate zone, and thus the stress regime in the fore-arc area cannot be properly modeled (this area was collapsed into the edge of the model). However, it is clear that a trench-parallel tension is produced near the tip of the plate, which possibly includes the fore-arc and the arc areas. This is in clear opposition with the N-S shortening derived from kinematic models [*Kley*, 1999; *Arriagada et al.*, 2008], but in agreement with the strain rates derived from GPS data [*Hindle et al.*, 2002]. The stress regime obtained when only the nonhydrostatic normal stress is imposed on the plate boundary favors the development of strike-slip faults radiating from the center of the curvature and the extrusion of the lithospheric plate rather than the formation of thrust faults (Figure 4c). Furthermore, the stress field does not favor the formation of the trench-parallel strike-slip systems north and south of the bend along the most oblique parts of the plate boundary since the second invariant of the deviatoric stress tensor J_2 is minimal in these locations (Figure 4c). This type of stress field is also obtained when both the nonhydrostatic normal stress and shear traction are imposed but the ratio of the shear stress over the nonhydrostatic normal stress is under a threshold value which depends on the 3-D geometry of the interplate zone.

[24] When the ratio of the shear stress over the nonhydrostatic normal stress is over the threshold value for the geometry of the plate boundary, the generated stress field is similar to that obtained when only the shear traction is imposed on the plate boundary in that a maximum trench-parallel compressive stress is generated near the center of the curvature and plate boundary (Figures 4d–4f). This is in agreement with the trench-parallel shortening structures in the fore-arc area in the center of the curvature [*Allmendinger et al.*, 2005], but the location of these structures in the coastal cordillera makes the comparison with experimental results difficult. In the arc and back-arc domains, no trench-parallel shortening has been clearly documented. GPS displacement pattern, fold and fault trends, as well as strike slip systems mostly exhibit radial shortening toward the foreland [*Hindle et al.*, 2005]. However, kinematic models of the orocline based on rotations from paleomagnetic data, shortening estimates from balanced cross sections, and variations of crustal cross-sectional area show convergence of the finite displacement vectors toward the axis of the

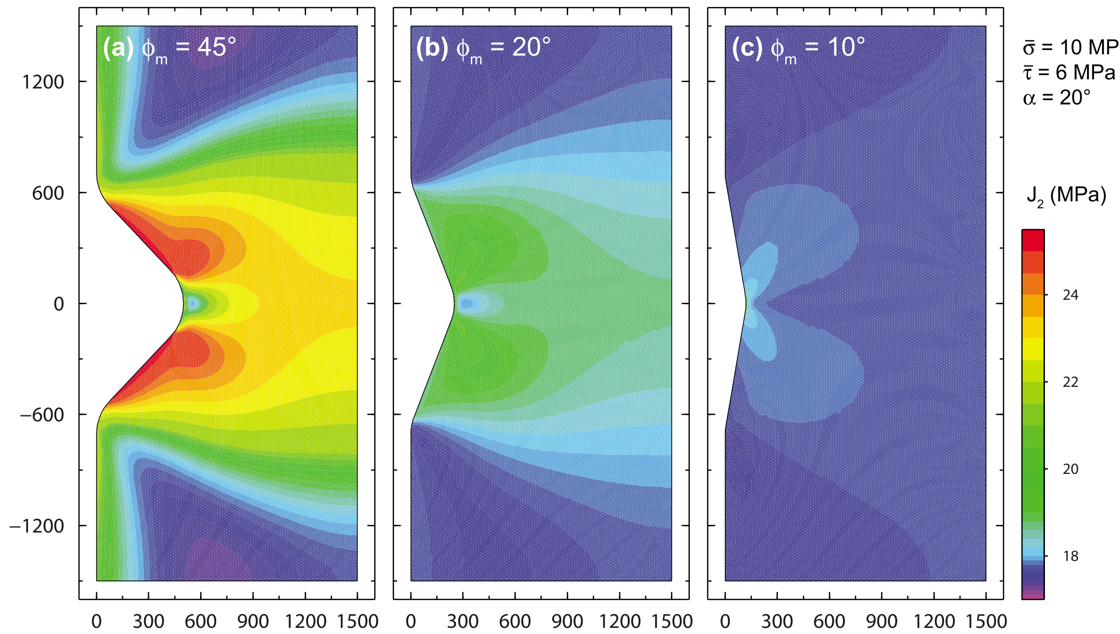

Figure 7. Variations of the distribution of the second invariant of the deviatoric stress tensor J_2 with variation of the maximum obliquity angle ϕ_m along the plate boundary. In the three runs, the dip angle of the plate boundary α is 20°, and the depth-averaged stress conditions are identical with the nonhydrostatic normal stress $\overline{\sigma}$ being 10 MPa and the shear traction $\overline{\tau}$ being 6 MPa (i.e., $\Omega = 0.6$). The geometry of the plate boundary is changed to test the influence of the maximum convergence obliquity angle ϕ_m, but the radius of curvature R and width W (see Figure 3) of the oblique section of the plate boundary are constant. (a) The maximum convergence obliquity angle ϕ_m is 45°; (b) ϕ_m is 20°; (c) ϕ_m is 10°. For each geometry of the plate boundary there is a threshold value Ω_l for which the transition between pattern 1 (generated by $\overline{\sigma}$ and obtained when $\Omega < \Omega_l$) and pattern 2 (generated by $\overline{\tau}$ and obtained when $\Omega > \Omega_l$) occurs. For $\phi_m = 45°$ and $\alpha = 20°$ (Figure 7), $\Omega_l = 0.4$ to 0.5; for $\phi_m = 20°$ and $\alpha = 20°$ (Figure 7b), $\Omega_l = 0.6$; For $\phi_m = 10°$ and $\alpha = 20°$ (Figure 7c), $\Omega_l = 0.7$.

bend [*Kley*, 1999; *Arriagada et al.*, 2008]. The first kinematic model [*Kley*, 1999] was also used to compute bulk strain rate tensors for long-term geological rates [*Hindle et al.*, 2002] and to perform crustal volume balancing [*Hindle et al.*, 2005]. The geological strain rate tensors agree with GPS-derived values for the direction of compression but reveal orogen-parallel shortening in the center of the bend in the arc/back-arc area, while GPS data show orogen-parallel extension. This dissimilarity could be interpreted as an artifact of the model, but the recent kinematic model by *Arriagada et al.* [2008] confirms this N-S shortening. Another interpretation is that the N-S deformation changed from compression to extension since the rise of the orogen, which suggests an increasing role of the body forces from the rise of the plateau or a more fundamental change in the tectonic regime of the orogen. However, one must also keep in mind that GPS data describe the actual displacement field at the surface of the orogen and may not represent the displacement field at depth. Our computations of the stress field are depth-averaged and thus rather correspond to stresses at depth. Comparison with the World Stress Map data [*Zoback et al.*, 1989; *Zoback*, 1992; *Fuchs and Müller*, 2001] is inconclusive since the map reveals both N-S extension and compression in the same areas of the central Andes. A possible reason may be that different methods used to assess the tectonic stress sampled the stress field at various depths. The orogen-parallel shortening in the arc and back-arc area of the central Andes, however, remains minor compared to the radial shortening. The estimated geological strain rates [*Hindle et al.*, 2002] are generally 1 order of magnitude lower in the trench parallel direction than in the trench-normal direction. Therefore the convergence of the finite displacement vector could be accommodated by a relatively minor trench-parallel slip component on generally N-S striking thrusts.

[25] Our models with the second pattern of J_2 (i.e., generated by $\overline{\tau}$; see Figures 4f, 5c, 6a, or 7a) also produce the most intense J_2 value along the most oblique edges of the plate boundary. In these areas, the least compressive horizontal stress becomes slightly compressional, and therefore a transpressional regime with a major horizontal slip component is expected. This corresponds to the generally NNE-SSW dextral faults (Atacama fault system [*Dewey and Lamb*, 1992; *Pelz*, 2000; *Gonzales et al.*, 2003], Precordilleran fault system [*Scheuber et al.*, 1995; *Reutter et al.*, 1996], Liquine-Ofqui fault system [*Cembrano et al.*, 2000, 2002; *Rosenau*, 2004]) observed south of the bend and the generally NNW-SSE sinistral faults (Incapulquio-El Castillo fault system [*Jacay et al.*, 2002; *Sempere et al.*, 2002]), north of it (Figure 1). In addition, the model predicts a rapid decrease of the second invariant away from the plate margin, which matches the position of these faults zones west of the arc and in the arc area.

[26] The model of the stress field generated by the shear traction thus matches several characteristic large-scale mechanical features of the central Andes (i.e., large E-W

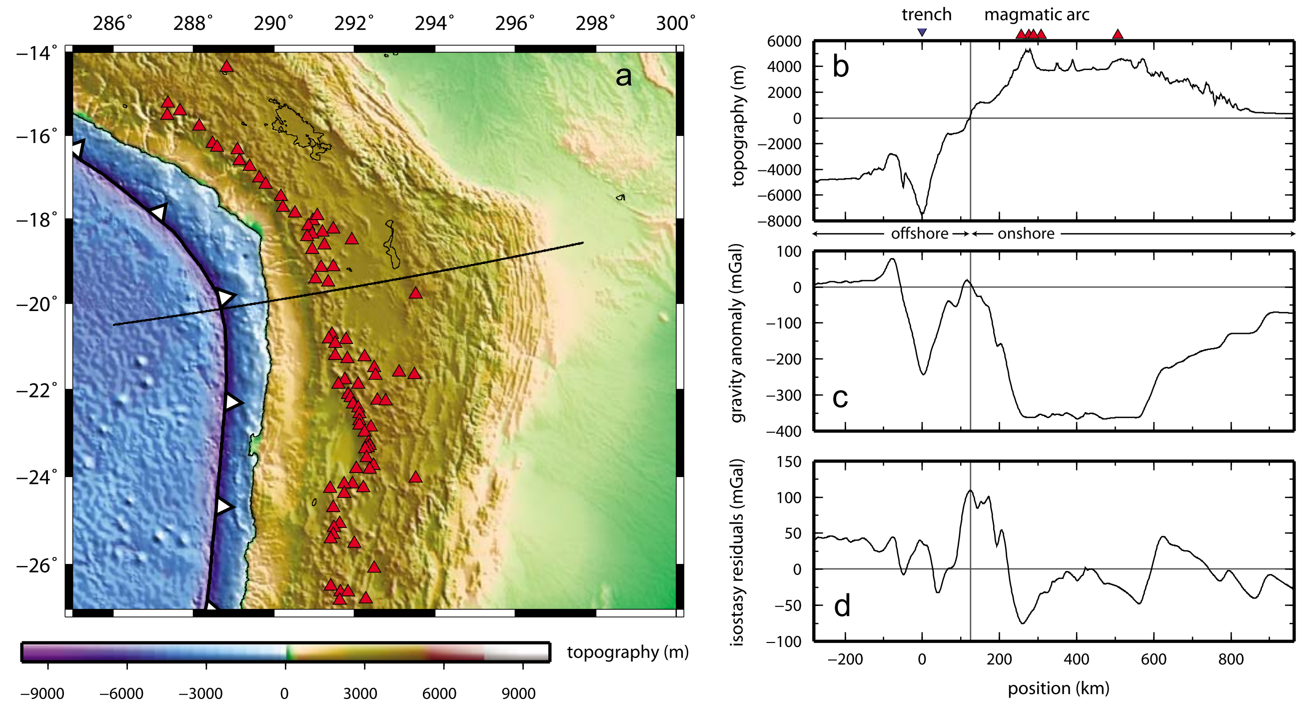

Figure 8. Geophysical profiles across the central Andes. (a) Map showing the location of the profiles. (b) Topographic profile marked by the deep trench and the high elevation of the Altiplano. (c) Gravity anomaly (mGal) composed of the free air anomaly offshore and the Bouguer anomaly onshore, revealing a large gravity low associated with large crustal thickness and thinned lithospheric mantle in the arc/back-arc area. (d) Isostasy residuals (mGal) showing that the main area not fitting the structural model is the fore arc where a small positive anomaly is present (gravity anomaly and isostasy residuals are from the SFB267 project [*Schmidt and Götze*, 2006]).

compression together with N-S compression in the center of the curvature and strike-slip systems along the most oblique parts of the plate boundary). Our results thus suggest that, since the N-S shortening is obtained in the kinematic models for the period 25 Ma to present [*Kley*, 1999; *Hindle et al.*, 2002, 2005; *Arriagada et al.*, 2008], the shear traction has dominated the stress conditions along the plate boundary (i.e., $\overline{\tau} > \Omega_1 \times \overline{\sigma}$) since 25 Ma.

4.2. Constraints on the Present-Day Interplate Stresses

[27] With an interplate zone geometry resembling the present-day South American plate boundary (Figure 9), the ratio between the shear traction and the nonhydrostatic normal stress must be greater than 0.6 to generate the trench-parallel compression in the center of the convex curvature. The present-day depth-averaged nonhydrostatic normal stress and shear traction can be estimated using the buoyancy stress generated by the high plateaus [*Froidevaux and Isacks*, 1984; *Lamb and Davis*, 2003; *Husson and Ricard*, 2004; *Lamb*, 2006] and the observation of a little positive gravity anomaly in the fore-arc area. For the Andes, computations yield a buoyancy stress of ~100 MPa [*Husson and Ricard*, 2004; *Lamb*, 2006]. The gravity anomaly in the central Andes presents a small positive gravity anomaly (~20 mGals) in the fore arc (Figure 8) [*Schmidt and Götze*, 2006]. This is significantly less than in the Kurils where a large positive anomaly in the fore arc (200 mGals) was interpreted as the signature of a high compressive nonhydrostatic normal stress on the plate boundary [*Shemenda*, 1993; *Tang and Chemenda*, 2000; *Tang et al.*, 2002]. It is, however, higher than in the Marianas where a negative gravity anomaly (~ −20 mGals) is observed in the fore arc and was interpreted as a high tensile nonhydrostatic normal stress on the plate boundary [*Shemenda*, 1994]. These signatures were, however, investigated for subduction zones with little shear traction because of the lubrication by sediments and fluids. In the central Andes, the weak positive gravity anomaly (Figure 8) can be interpreted as either the signature of a weakly compressive nonhydrostatic normal stress, or of a moderate to high compressive stress counterbalanced by the high shear traction. The vertical component of the force F_n generated by the nonhydrostatic normal stress drives the fore-arc area upward and thus produces the positive gravity anomaly. However, the vertical component of the force F_f due to the shear traction drives the fore arc downward and can therefore counterbalance the vertical effect of the nonhydrostatic normal stress.

[28] The isostasy residuals show a little positive peak suggesting that the vertical component of F_n may be greater than the vertical component of F_f, but the low magnitudes of the gravity anomaly and isostasy residuals suggest that the vertical force components must be of the same magnitude (Figure 8). This interpretation is in agreement with the observation of a correlation between the trench-parallel low in the gravity signal, long-term subsidence in the fore-arc area, and the occurrence of large earthquakes along the plate boundary, interpreted as areas of higher levels of coupling between the plates [*Song and Simons*, 2003]. With a

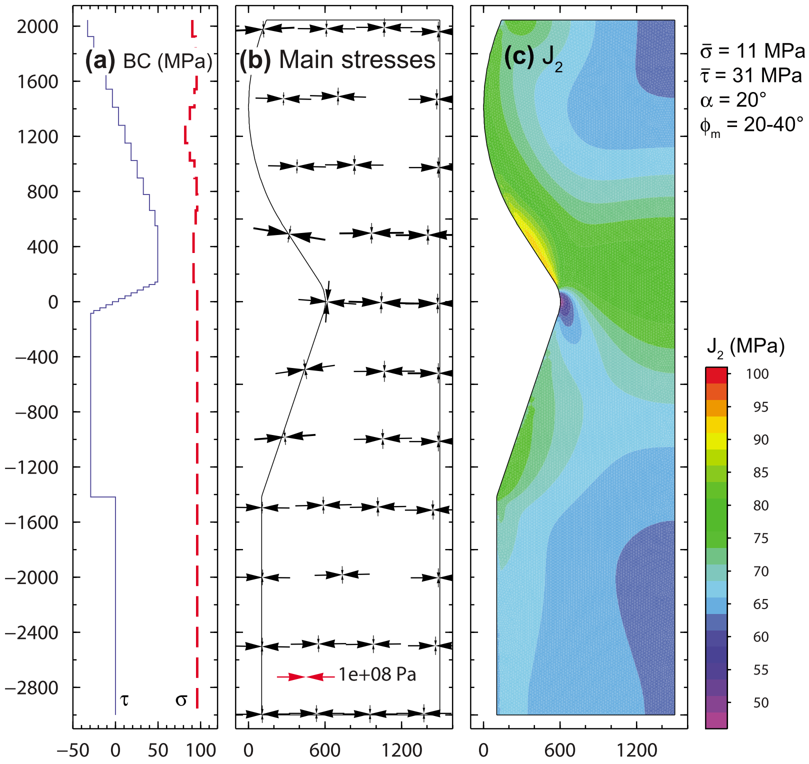

Figure 9. Experimental results obtained for a plate boundary geometry resembling the present-day South American margin with a dip angle of 20°, a depth-averaged shear traction of 31 MPa, and a depth-averaged nonhydrostatic normal stress of 11 MPa. The second invariant of the deviatoric stress tensor is larger along the most oblique section of the plate boundary, which is directly north of the bend. The largest trench-parallel compression is obtained near the center of the seaward-concave curvature.

buoyancy stress σ_b of ~100 MPa [*Lamb*, 2006], we found that a depth-averaged shear traction of 31 MPa and a depth-averaged nonhydrostatic normal stress of 11 MPa allow balancing of the horizontal stresses and vertical force components on a plate boundary inclined at 20°:

$$(F_f)_{hn}/S + (F_n)_h/S = \sigma_b$$

$$(F_f)_v + (F_n)_v = 0$$

[29] These values are in agreement with previous estimations [*Husson and Ricard*, 2004; *Lamb*, 2006]. The stress distribution obtained with these values is presented in Figure 9. The ratio of the shear traction over the nonhydrostatic normal stress (Ω = 2.8) is well above the threshold ratio (Ω_l = 0.6) and thus generates a pattern of J_2 of the second type with large horizontal shear stress along the most oblique part of the plate boundary and N-S compression of 75 MPa together with a E-W compression of 97 MPa in the center of the seaward-concave curvature (Figure 9).

[30] Our results thus suggest that the buoyancy stress generated by the plateaus is supported by a large shear traction on the plate boundary and a little compressive nonhydrostatic normal stress. This situation must generate today a N-S compression in the center of the seaward curvature of the plate boundary.

4.3. Geodynamical Significance of the Stress Conditions Along the Interplate Zone Generating the Trench-Parallel Compression

[31] We first assume that the plate boundary is characterized by an existing seaward-concave curvature. In this case, we found that the ratio Ω of the shear traction to nonhydrostatic normal stress is a major parameter controlling whether the trench-parallel stress in the center of the curvature is a tension or compression. The ratio must be above a threshold value Ω_l in order to generate the N-S shortening in the center of the curvature. Ω depends on the level of interplate coupling which modulates the magnitude of the shear traction. Therefore a high interplate coupling (through, for example, a lack of sediment in the trench) indeed favors the formation of thrusts with minor strike-slip component in the center of an existing curvature and strike-slip faults along the oblique segments of this curvature. A series of experiments with $\overline{\tau}$ increasing from 0 to 10 MPa, while $\overline{\sigma}$ is kept constant at 10 MPa (Ω increases from 0 to 1) is presented in Figure 10a. For the employed geometry (ϕ_m = 45°, α = 30°), this increase in interplate shear traction leads to a switch from a N-S tension in the center of the curvature to a N-S compression, and a switch from the first to the second pattern of J_2 with high shear stress

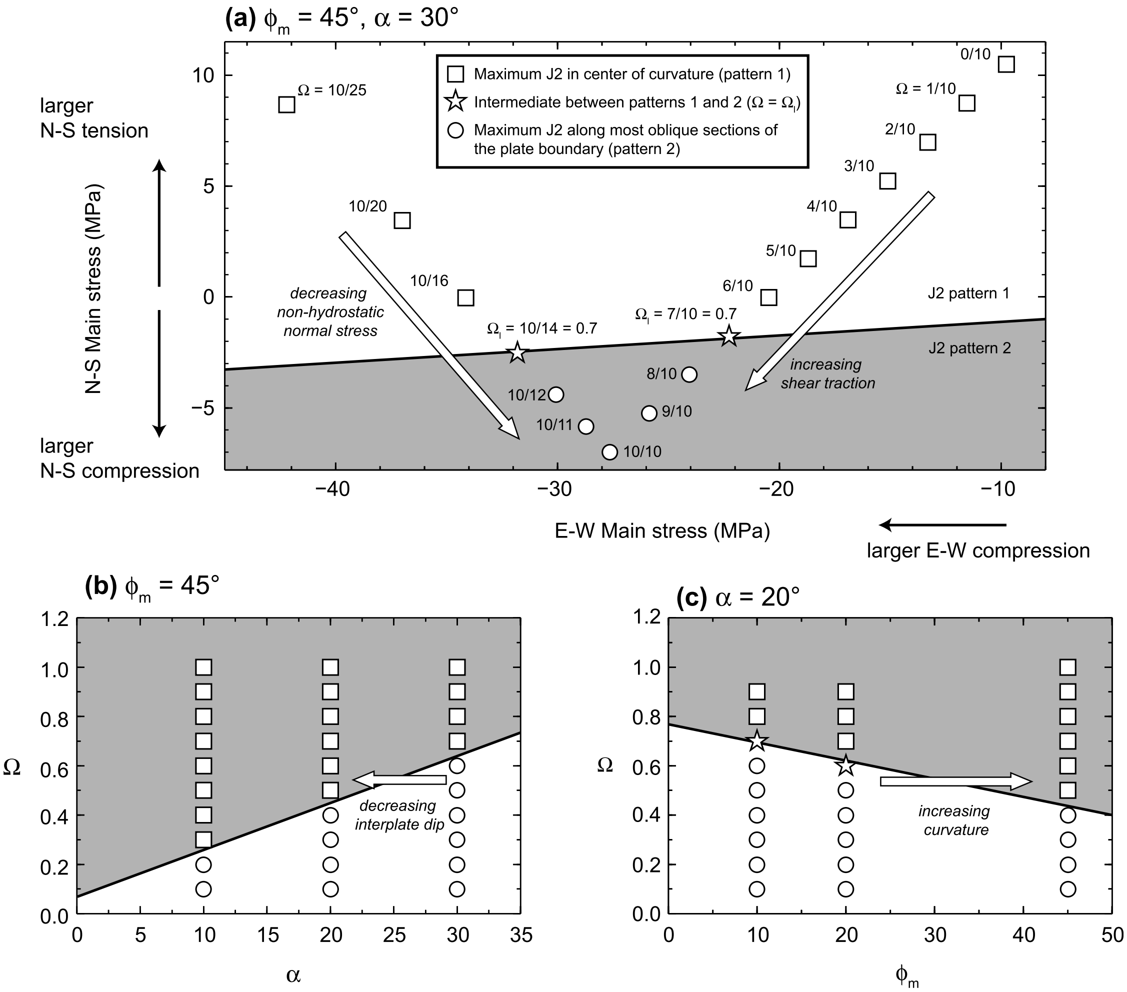

Figure 10. Graphs of experimental runs and main mechanical results. (a) Plot of two series of experimental runs for which the geometry of the plate boundary is constant and either the nonhydrostatic normal stress or shear traction change. The runs are plotted with respect to the produced E-W and N-S main stresses. Ratios near the points give the employed values of $\overline{\tau}$ and $\overline{\sigma}$. The gray-shaded domain represents the domain in which the produced stress field is similar to that produced by the shear traction. The white arrows show two possible geodynamic scenarios (increase of $\overline{\tau}$ or decrease of $\overline{\sigma}$) leading to a switch to the second pattern of J_2 and establishment of N-S compression in the center of the curvature. Figure 10 shows that various stress conditions with similar ratios Ω result in similar N-S main stress in the center. (b) Plots of the experimental runs for a constant maximum obliquity angle ϕ_m (see Figure 3) but varying stress conditions (Ω) and interplate zone dip angle (α). Circles, stars, boxes, and the gray-shaded domain have the same significance as in Figure 10a. The white arrow shows a geodynamic scenario in which the interplate dip angle decreases but the stress conditions do not change (Ω = const), which leads to producing the second pattern of J_2 and N-S compression in the center of the seaward curvature. (c) Similar plot as in Figure 10b, but the dip angle is constant, and the maximum obliquity angle changes. The white arrow shows a scenario in which the curvature increases, and therefore the maximum obliquity angle increases, while the stress conditions are constant (Ω = const). This evolution leads to producing the second pattern of J_2 and N-S compression in the center of the curvature.

along the most oblique sections of the plate boundary. However, other mechanical properties of the subducting plate can also change Ω. A low flexural rigidity of the subducting lithosphere produces a small nonhydrostatic normal stress, while a high slab pull force can reduce this compressive nonhydrostatic normal stress or even generate a tensile nonhydrostatic stress [*Shemenda*, 1993]. Therefore, low flexural rigidity or high slab pull force also favor trench-parallel compression in the center of the curvature. The slab pull force, however, must not be too high, otherwise it would generate trench-normal tension in the arc area instead of compression [*Shemenda*, 1993]. This threshold limit of the slab pull force has not been investigated in this study. Finally, flow in the asthenospheric mantle around the subducting slab can also produce an additional pressure on the upper or lower surfaces of the slab, which would increase or decrease, respectively, the nonhydrostatic normal stress on the interplate zone

[*Shemenda*, 1993; *Boutelier and Cruden*, 2008]. A decrease of the nonhydrostatic normal stress with other parameters being constant is presented in Figure 10a with a series of experiments in which $\overline{\sigma}$ decreases from 25 to 10 MPa while $\overline{\tau}$ is kept constant at 10 MPa. The decrease of $\overline{\sigma}$ leads to a larger N-S compression or a smaller N-S tension in the center of the seaward-concave curvature. This series of experiments also show that a decrease of $\overline{\sigma}$ generates a decrease of the E-W compression in the center of the seaward-concave curvature (Figure 10a), in agreement with laboratory results [*Shemenda*, 1993].

[32] For a particular geometry of the plate boundary there are multiple combinations of shear traction and nonhydrostatic normal stress generating a trench-parallel compression in the center of the seaward-concave curvature (see Figure 10a). The nature of the plate contact (lubricated or not) is an important parameter because it influences the shear traction. However, equally important are the dynamics of the subducting lithosphere and kinematics of the overriding plate which control the sign and magnitude of the nonhydrostatic normal stress on the interplate zone.

4.4. Evolution of the Plate Boundary Geometry

[33] We interpret the N-S shortening in the center of the seaward concave curvature of the plate boundary in the central Andes as the signature of a boundary condition dominated by shear traction. However, the stress distribution is also controlled by the geometry of the plate boundary, which has changed through time. The magnitudes of the horizontal components of the forces generated by the nonhydrostatic normal stress and shear stress depend on both the dip angle and the obliquity of the convergence. It follows that the evolution with time of the interplate zone dip angle induces a change of the produced stress field. For example, if the dip angle of the interface between the plates decreases with time, a stronger N-S compression is produced in the center of the curvature without any other change of the boundary conditions. At present, however, this evolution remains largely unknown. Slab dip at depth was shown to correlate with the shallow slab dip [*Lallemand et al.*, 2005], and therefore slab dip may be used as a proxy for the dip of the interplate zone; however, slab dip evolution is also poorly known. The only temporal constraint of slab dip evolution is obtained from the spatial distribution of volcanism chemistry and ore deposits [*Allmendinger et al.*, 1997; *Mahlburg Kay et al.*, 1999; *Mahlburg Kay and Mpodozis*, 2001] and suggests a flat-slab episode in the central Andes at 33–26 Ma. In this scenario, the average dip angle would appear shallower, which allows generating the largest N-S compression in the center of the seaward-concave curvature for lower values of the threshold ratio Ω. This evolution of the dip angle while other parameters are maintained constant is presented in Figure 10b. A decrease of the averaged dip angle as proposed for a stage of flat slab subduction in the central Andes in early Miocene would shift the system toward the domain characterized by the second pattern of J_2 and generating a N-S compression in the center of the seaward-concave curvature.

[34] The evolution of the plate convergence obliquity and geometry of the curvature is better constrained than the evolution of the interplate dip-angle. Kinematic models of the central Andes [*Kley*, 1999: *Arriagada et al.*, 2008] include an increase of curvature of the plate boundary. This evolution, which is still presently active, also induces a change in the stress field (Figure 10c). With increasing convergence obliquity along the sides of a growing curvature, more N-S compression is generated in the center of the curvature, and more horizontal shearing is produced along the most oblique parts of the plate boundary. Without invoking the change of any parameter other than the obliquity of the convergence, our results show that during the formation of the curvature of the plate boundary of the central Andes, the influence of the shear traction on the stress field generated in the overriding plate has increased (Figure 7).

4.5. Consequences for the Candidate Mechanisms for Orocline Bending and Formation of the High Plateaus

[35] The effects of the nonhydrostatic normal stress and shear traction on a curved plate boundary presented in this study bring about new constraints on the candidate mechanism for orocline bending and plateau formation. Clearly, a large E-W tectonic shortening happened in the central Andes [*Oncken et al.*, 2006]; however, whether this E-W compression was generated by an increase of the nonhydrostatic normal stress or shear traction remained unclear. For example, 3-D numerical experiments have shown that the length of the trench has a significant impact on the dynamics of the subducted lithosphere, and in the case of a long trench, as in South America, the center is fixed while the edges retreat [*Schellart et al.*, 2007]. Combined with the westward drift of the South American plate this leads *Schellart et al.* [2007] to propose that the large shortening in the central Andes is due to the geometry of the slab, which is controlled by the length of the trench. However, if the interplate friction is low and the main stress on the plate boundary is a high compressive nonhydrostatic normal stress, then only this nonhydrostatic normal stress is locally significantly increased by the westward drift of South America. This would generate the observed E-W shortening and the formation of a curvature, but it would also tend to produce a N-S tension in the developing seaward-concave area. A similar analysis can be conducted with the hypothesis that westward flow in the mantle drags the slab westward in the center of the plate boundary [*Russo and Silver*, 1994, 1996]. If this process only locally increases the nonhydrostatic normal stress because the interplate friction coefficient is very low, then it would not be able to generate the observed N-S shortening in the center of the curvature and the transcurrent fault systems along the most oblique sections of the plate boundary [*Jacay et al.*, 2002; *Sempere et al.*, 2002].

[36] These two mechanisms would, however, be effective if the interplate friction coefficient was raised because, for example, of the lack of sediments entering the trench [*Bangs and Cande*, 1997; *Lamb*, 2006]. Slab retreat near the edges of the plate boundary with slab anchorage near the center [*Schellart et al.*, 2007] or flow in the mantle [*Russo and Silver*, 1994, 1996] can increase the nonhydrostatic normal stress and thus drive the bending of the orocline. If the ratio Ω of the shear traction over the nonhydrostatic normal stress remains larger than the threshold value Ω_1 associated with the plate geometry, the large shear traction along the oblique sections would produce the N-S shortening near the symmetry axis of the curvature. Then with increasing curvature

the influence of the shear traction on the developed stress field would further increase. Finally, if the geometry of the plate margin participates in driving the bending through enhanced interplate friction, then it can also generate the excess in situ rotations revealed by the reconstruction of the plate margin geometry of *Arriagada et al.* [2008].

[37] Topographic features such as oceanic ridges and plateaus carried by the subducting lithosphere have been proposed to control the deformation regime in the upper plate [*Giese et al.*, 1999; *Gutscher et al.*, 2000; *Yanez et al.*, 2001]. However, the large-scale lateral continuity of the structures accommodating the large E-W shortening and the synchronicity of their formations suggest that ridges and plateaus are not capable of driving the deformation in the arc/back-arc domain because they lack both the lateral extend and longevity [*Oncken et al.*, 2006]. In contrast, the lateral variations of slab dip exhibit the proper spatial scale. A "flat slab" subduction stage was also proposed for the central Andes in early Miocene based on the pattern of magmatism and ore deposits [*Allmendinger et al.*, 1997; *Mahlburg Kay et al.*, 1999; *Mahlburg Kay and Mpodozis*, 2001]. To this period corresponds an increase in the bulk shortening rate in the central Andes and a shift of the shortening toward the back-arc domain [*Oncken et al.*, 2006]. This eastward shift of the deformation clearly demonstrates that the horizontal E-W shortening was driven by the shear traction on the interplate zone since this zone was then very shallow, and the force F_n resulting from the nonhydrostatic normal stress must have been nearly vertical. In this geodynamic framework of a flat slab or very shallow dipping subduction zone, and of E-W shortening driven by shear traction, our results suggest that the largest N-S compression and thus shortening would have been produced in the center of the seaward-concave curvature even if this curvature was mild. Furthermore, the flat slab geometry would shift the N-S shortening with the E-W shortening to the Eastern Cordillera as in the kinematic models [*Kley*, 1999; *Arriagada et al.*, 2008]. This "flat slab" stage is followed by a stage of steepening of the slab in middle Miocene promoting the melting of the overlying hydrated mantle and lower crust and thus thermal weakening of the upper plate [*Mahlburg Kay and Mpodozis*, 2001]. Our results suggest that the slab steepening, if accompanied by a steepening of the plate interface, produces a shift in the system toward smaller N-S compression in the center of the curvature (Figure 10b). However, this shift may not lead to N-S tension if the ratio of the shear traction over the nonhydrostatic normal stress was sufficiently high. Another possibility is that the depth-averaged dip angle of the interplate zone did not increase sufficiently to switch from N-S compression to N-S tension. The observation that subduction erosion has dominated mass transfer in the fore arc during Cenozoic [*Kukowski and Oncken*, 2006], and the present-day relatively shallow angle of the interplate zone in the central Andes [*Cahill and Isacks*, 1992], suggest that both the ratio of the shear traction over nonhydrostatic normal stress was high, and the reduction of the interplate dip angle was low. Finally, the weakening of the upper plate in the central Andes due to the heating associated with the slab steepening would have allowed a larger E-W shortening [*Sobolev et al.*, 2006] and thus an increase of the curvature of the plate boundary which in turn favors larger N-S compression (Figure 10c).

[38] *Iaffaldano et al.* [2006] and *Iaffaldano and Bunge* [2008] proposed that the buildup of the high plateaus had a large impact on global plate tectonics and slowed down the convergence between Nazca and South America by increasing the normal stress on the interplate zone. Our results suggest that the subduction system had to be in a regime where the ratio Ω is sufficiently high that despite this increase of nonhydrostatic normal stress (and thus a decrease of Ω), this ratio remained above the threshold value, and the stress regime remained dominated by the effect of the shear traction.

5. Conclusions

[39] In this study we have shown that a trench-parallel compression in the center of a seaward-concave curved plate boundary as observed in the kinematic models of the Andes can be produced by the stress conditions along the interplate zone. The trench-parallel horizontal component of the force due to the shear traction is responsible for the lateral drag of the fore arc toward the center of the curvature. It then produces a trench-parallel compression. However, to be dominant, this effect must be greater than the action of the trench-normal component of the same force, and the horizontal component of the force generated by the nonhydrostatic normal stress, which both act in the opposite direction. It follows that both the stress conditions on the plate boundary and the 3-D geometry of the interface between the plates control whether the trench-parallel stress in the center of a seaward-concave curvature is a tension or compression. Low dip angle and high convergence obliquity favor the realization of the trench-parallel compression in the center of the curvature.

[40] The observation of trench-parallel shortening in the center of the curvature, together with large horizontal slip north and south of the bend in the Andes, suggest in the light of our modeling results that the effect of shear traction along the interplate zone was dominant during the buildup of the orogen. This could have been achieved with a high shear traction and/or low compressive nonhydrostatic normal stress on the plate boundary.

[41] Estimations of the depth-averaged shear traction and nonhydrostatic normal stress using the buoyancy stress generated by the high plateaus and the observation of a weak gravity anomaly in the fore arc suggest that the plateaus are currently supported by large shear traction on the plate boundary and little compressive nonhydrostatic normal stress. These stress boundary conditions imposed on a plate boundary resembling the present-day shape of the South American margin generate a trench-parallel compression in the center of the curvature. We have shown that the effect of the shear traction on the generated stress field in the overriding plate must have increased during the buildup of the orogeny because of the development of the curvature of the plate boundary.

[42] Finally, our results bring a new constraint on the proposed mechanisms for the formation of the curvature and buildup of the orogen. An increase of E-W shortening in the central Andes associated with an increase of nonhydrostatic

normal stress on the plate boundary must be moderated by the observation of the N-S shortening in the kinematic models of the Andes since 25 Ma.

[43] According to our results, this observation does not exclude the hypothesis of an increase of the nonhydrostatic normal stress but sets a new limit to the magnitude of this increase, as the effect of the shear traction on the interplate zone has remained dominant.

[44] **Acknowledgments.** Constructive comments by anonymous reviewers and the Associate Editor greatly improved the manuscript. Funding was provided by an Alexander von Humboldt foundation grant to D.B.

References

Allmendinger, R., T. Jordan, S. Kay, and B. Isacks (1997), The evolution of the Altiplano Puna plateau of the central Andes, *Annu. Rev. Earth Planet. Sci.*, *25*, 139–174, doi:10.1146/annurev.earth.25.1.139.

Allmendinger, R., G. Gonzales, J. Yu, G. Hoke, and B. Isaacks (2005), Trench-parallel shortening in the northern Chilean forearc: Tectonic and climatic implications, *GSA Bull*, *117*, 89–104, doi:10.1130/B25,505.1.

Arriagada, C., P. Roperch, C. Mpodozis, and P.R. Cobbold (2008), Paleogene building of the Bolivian Orocline: Tectonic restoration of the central Andes in 2-D map view, *Tectonics*, *27*, TC6014, doi:10.1029/2008TC002269.

Ave Lallemant, H. (1996), Displacement partitioning and arc-parallel extension in the Aleutian volcanic island arc, *Tectonophysics*, *256*, 279–293, doi:10.1016/0040-1951(95)00171-9.

Bangs, N., and S. C. Cande (1997), Episodic development of a convergent margin inferred from structures and processes along the southern Chile margin, *Tectonics*, *16*, 489–503, doi:10.1029/97TC00494.

Beck, M. E. (1998), On the mechanism of crustal block rotations in the central Andes, *Tectonophysics*, *299*, 75–92, doi:10.1016/S0040-1951(98)00199-1.

Beck, S., and G. Zandt (2002), The nature of orogenic crust in the central Andes, *J. Geophys. Res.*, *107*(B10), 2230, doi:10.1029/2000JB000124.

Bonnardot, M.-A., R. Hassani, E. Tric, E. Ruellan, and M. Regnier (2008), Effect of margin curvature on plate deformation in a 3-D numerical model of subduction zones, *Geophys. J. Int.*, *173*, doi:10.1111/j.1365-246X.2008.03752.x.

Boutelier, D. (2004), La modélisation expérimentale tridimensionnelle thermomécanique de la subduction continentale et l'exhumation des roches de ultra-haute pression/basse temperature, Ph.D. thesis, Univ. de Nice-Sophia Antipolis, Nice, France.

Boutelier, D., and A. Cruden (2008), Impact of regional mantle flow on subducting plate geometry and interplate stress: Insights from physical modelling, *Geophys. J. Int.*, *174*, 719–732, doi:10.1111/j.1365-246X.2008.03,826.x.

Cahill, T., and B. Isacks (1992), Seismicity and shape of the subducted Nazca plate, *J. Geophys. Res.*, *97*, 17,503–17,529, doi:10.1029/92JB00493.

Cembrano, J., E. Schermer, A. Lavenu, and A. Sanhueza (2000), Contrasting nature of deformation along an intra-arc shear zone, the Liquine-Ofqui fault zone, southern Chilean Andes, *Tectonophysics*, *319*, 129–149, doi:10.1016/S0040-1951(99)00321-2.

Cembrano, J., A. Lavenu, P. Reynolds, G. Arancibia, G. Lopez, and A. Sanhueza (2002), Late Cenozoic transpressional ductile deformation north of the Nazca-South America-Antarctica triple junction, *Tectonophysics*, *354*, 289–314, doi:10.1016/S0040-1951(02)00388-8.

Chemenda, A., S. Lallemand, and A. Bokun (2000), Strain partitioning and interplate friction in oblique subduction zones: Constraints provided by experimental modeling, *J. Geophys. Res.*, *105*, 5567–5581, doi:10.1029/1999JB900332.

DeMets, C., R. G. Gordon, D. F. Argus, and S. Stein (1994), Effect of recent revisions to the geomagnetic reversal time scale on estimates of current plate motions, *Geophys. Res. Lett.*, *21*, 2191–2194.

Dewey, J., and S. Lamb (1992), Active tectonics of the Andes, *Tectonophysics*, *205*, 79–95.

Dickinson, W. (2004), Evolution of the North American cordillera, *Annu. Rev. Earth Planet. Sci.*, *32*, 13–45, doi:10.1146/annurev.earth.32.101802.120257.

Fitch, T. (1972), Plate convergence, transcurrent faults, and internal deformation adjacent to southeast Asia and the western pacific, *J. Geophys. Res.*, *77*, 4432–4460, doi:10.1029/JB077i023p04432.

Franz, G., F. Lucassen, W. Kramer, R. Trumbull, R. Romer, H.-G. Wilke, J. Viramonte, R. Becchio, and W. Siebel (2006), Crustal evolution at the central Andean continental margin: A geochemical record of crustal growth, recycling and destruction, in *The Andes: Active Subduction Orogeny, Frontiers Earth Sci.*, vol. XXII, edited by O. Oncken et al., pp. 45–64, Springer, Berlin.

Froidevaux, C., and B. Isacks (1984), The mechanical state of the lithosphere in the Altiplano-Puna segment of the Andes, *Earth Planet. Sci. Lett.*, *71*, 305–314, doi:10.1016/0012-821X(84)90095-5.

Fuchs, K., and B. Müller (2001), World stress map of the Earth: A key to tectonic processes and technological applications, *Naturwissenschaften*, *88*, 357–371, doi:10.1007/s001140100253.

Gephart, J. (1994), Topography and subduction geometry in the central Andes: Clues to the mechanics of a noncollisional orogen, *J. Geophys. Res.*, *99*, 12,279–12,288, doi:10.1029/94JB00129.

Giese, P., E. Scheuber, F. Schilling, M. Schmitz, and P. Wigger (1999), Crustal thickening processes in the central Andes and the different natures of the Moho-discontinuity, *J. South Am. Earth Sci.*, *12*, 201–220, doi:10.1016/S0895-9811(99)00014-0.

Gonzales, G., J. Cembrano, D. Carrizo, A. Macci, and H. Schneider (2003), Link between forearc tectonics and Pliocene-Quaternary deformation of the Coastal Cordillera, northern Chile, *J. South Am. Earth Sci.*, *16*, 321–342, doi:10.1016/S0895-9811(03)00100-7.

Gudmundsson, O., and M. Sambridge (1998), A regionalized upper mantle (RUM) seismic model, *J. Geophys. Res.*, *103*, 7121–7136, doi:10.1029/97JB02488.

Gutscher, M. A., W. Spakman, H. Bijwaard, and E. R. Engdahl (2000), Geodynamics of flat subduction: Seismicity and tomographic constraints from the Andean margin, *Tectonics*, *19*, 814–833, doi:10.1029/1999TC001152.

Hartley, A. (2003), Andean uplift and climate change, *J. Geol. Soc.*, *160*, 7–10, doi:10.1144/0016-764902-083.

Haschke, M., and A. Günther (2003), Balancing crustal thickening in arcs by tectonic vs. magmatic means, *Geology*, *31*, 933–936, doi:10.1130/G19945.1.

Hassani, R., D. Jongmans, and J. Chéry (1997), Study of plate deformation and stress in subduction processes using two-dimensional numerical models, *J. Geophys. Res.*, *102*(B8), 17,951–17,966.

Hindle, D., J. Kley, E. Klosko, S. Stein, T. Dixon, and E. Norabuena (2002), Consistency of geologic and geodetic displacements during Andean orogenesis, *Geophys. Res. Lett.*, *29*(8), 1188, doi:10.1029/2001GL013757.

Hindle, D., J. Kley, O. Oncken, and S. Sobolev (2005), Crustal balance and crustal flux from shortening estimates in the central Andes, *Earth Planet. Sci. Lett.*, *230*, 113–124, doi:10.1016/j.epsl.2004.11.004.

Horton, B. (1999), Erosional control on the geometry and kinematics of thrust belt development in the central Andes, *Tectonics*, *18*, 1292–1293, doi:10.1029/1999TC900051.

Husson, L., and Y. Ricard (2004), Stress balance above subduction: Application to the Andes, *Earth Planet. Sci. Lett.*, *222*, 1037–1050, doi:10.1016/j.epsl.2004.03.041.

Hyndman, R., C. Currie, and S. Mazzotti (2005), Subduction zone backarcs, mobile belts, and orogenic heat, *GSA Today*, *15*, 4–10, doi:10:1130/1052-5173(2005)015.

Iaffaldano, G. and H-P. Bunge (2008), Strong plate coupling along the Nazca-South America convergent margin, *Geology*, *36*, 443–446, doi:10.1130/G24489A.

Iaffaldano, G., H.-P. Bunge, and T. Dixon (2006), Feedback between mountain belt growth and plate convergence, *Geology*, *34*, 893–896, doi:10.1130/G22661.1.

Isacks, B. (1988), Uplift of the central Andean plateau and the bending of the Bolivian orocline, *J. Geophys. Res.*, *93*, 3211–3231, doi:10.1029/JB093iB04p03211.

Jacay, J., T. Sempere, L. Husson, and A. Pino (2002), Structural characteristics of the Incapuquio fault system, southern Peru, paper presented at the V International Symposium on Andean Geodynamics, IRD, Toulouse, France, 16–18 September.

Jarrard, R. (1986a), Terrane motion by strike-slip faulting of forearc slivers, *Geology*, *14*, 780–783.

Jarrard, R. (1986b), Relations among subduction parameters, *Rev. Geophys.*, *24*, 217–284.

Jordan, T., B. Isacks, R. Allmendinger, J. Brewer, V. Ramos, and C. Ando (1983), Andean tectonics related to geometry of subducted Nazca plate, *Geol. Soc. Am. Bull.*, *94*, 341–361, doi:10.1130/0016-7606(1983)94<341:ATRTGO>2.0.CO;2.

Kay, R. and S. M. Kay (1993), Delamination and delamination magnetism, *Tectonophysics*, *219*, 177–189, doi:10.1016/0040-1951(93)90295-U.

Kley, J. (1999), Geologic and geometric constraints on a kinematic model of the Bolivian orocline, *J. South Am. Earth Sci.*, *12*, 221–235, doi:10.1016/S0895-9811(99)00015-2.

Kley, J., and C. Monaldi (1998), Tectonic shortening and crustal thickness in the central Andes: How good is the correlation?, *Geology*, *26*, 723–726, doi:10.1130/0091-7613(1998)026<0723:TSACTI>2.3.CO;2.

Kley, J., C. Monaldi, and J. Salfity (1999), Along-strike segmentation of the Andean foreland: Causes and consequences, *Tectonophysics*, *301*, 75–94, doi:10.1016/S0040-1951(98)90223-2.

Kukowski, N., and O. Oncken (2006), Subduction erosion at the Chile-Peru margin, in *The Andes: Active Subduction Orogeny, Frontiers Earth Sci.*, vol. XXII, edited by O. Oncken et al., pp. 217–236, Springer, Berlin.

Lallemand, S., A. Heuret, and D. Boutelier (2005), On the relationships between slab dip, back-arc stress, upper plate absolute motion, and crustal nature in subduction zones, *Geochem. Geophys. Geosyst.*, *6*, Q09006, doi:10.1029/2005GC000917.

Lamb, S. (2001), Vertical axis rotation in the Bolivian orocline, South America: 1. Paleomagnetic analysis of Cretaceous and Cenozoic rocks, *J. Geophys. Res.*, *106*, 26,605–26,632, doi:10.1029/2001JB900012.

Lamb, S. (2006), Shear stresses on megathrusts: Implications for mountain building behind subduction zones, *J. Geophys. Res.*, *111*, B07401, doi:10.1029/2005JB003916.

Lamb, S., and P. Davis (2003), Cenozoic climate change as a possible cause for the rise of the Andes, *Nature*, *425*, 792–797, doi:10.1038/nature02049.

Mahlburg Kay, S., and C. Mpodozis (2001), Central Andean ore deposits linked to evolving shallow subduction systems and thickening crust, *GSA Today*, *11*, 4–9.

Mahlburg Kay, S., C. Mpodozis, and B. Coira (1999), Neogene magmatism, tectonism, and mineral deposits of the central Andes (22° to 33°S latitude), *Soc. Econ. Geol. Spec. Publ.*, *7*, 27–59.

McCaffrey, R. (1991), Slip vectors and stretching of the Sumatran fore arc, *Geology*, *19*, 881–884, doi:10.1130/0091-7613(1991)019<0881:SVASOT>2.3.CO;2.

McCaffrey, R. (1992), Oblique plate convergence, slip vectors, and forearc deformation, *J. Geophys. Res.*, *97*, 8905–8915, doi:10.1029/92JB00483.

McCaffrey, R. (1996), Estimates of modern arc-parallel strain rates in fore arcs, *Geology*, *24*, 27–30, doi:10.1130/0091-7613(1996)024<0027:EOMAPS>2.3.CO;2.

McCaffrey, R., and J. Nabalek (1998), Role of oblique convergence in the deformation of the Himalayas and southern Tibet plateau, *Geology*, *26*, 691–694, doi:10.1130/0091-7613(1998)026<0691:ROOCIT>2.3.CO;2.

Molnar, P., and T. Atwater (1978), Interarc spreading and Cordilleran tectonics as alternates related to the age of subducted oceanic lithosphere, *Earth Planet. Sci. Lett.*, *41*, 330–340, doi:10.1016/0012-821X(78)90187-5.

Molnar, P., and P. England (1990), Temperatures, heat flux, and frictional stress near major thrust faults, *J. Geophys. Res.*, *95*, 4833–4856, doi:10.1029/JB095iB04p04833.

Montgomery, D., G. Balco, and S. Willett (2001), Climate, tectonics, and the morphology of the Andes, *Geology*, *29*, 579–582, doi:10.1130/0091-7613(2001)029<0579:CTATMO>2.0.CO;2.

Oncken, O., D. Hindle, J. Kley, K. Elger, P. Victor, and K. Schemmann (2006), Deformation of the central Andean upper plate system: Facts, fiction, and constraints for plateau models, in *The Andes: Active Subduction Orogeny, Frontiers Earth Sci.*, vol. XXII, edited by O. Oncken et al., pp. 3–27, Springer, Berlin.

Peacock, S. (1996), Thermal and petrologic structure of subduction zones, in Subduction: Top to Bottom, *Geophys. Monogr. Ser.*, *96*, 119–133.

Pelz, K. (2000), Tectonic erosion along the central Andean forearc (20–24°S), Ph.D. thesis, *Sci. Tech. Rep. STR00/20*, GeoForschungsZentrum, Potsdam.

Raymo, M., and W. Ruddiman (1992), Tectonic forcing of late Cenozoic climate, *Nature*, *359*, 117–122, doi:10.1038/359117a0.

Reutter, K.-J., E. Scheuber, and G. Chong (1996), The Precordilleran fault system of Chuquicamata, northern Chile: Evidence for reversals along arc-parallel strike-slip faults, *Tectonophysics*, *259*, 213–228, doi:10.1016/0040-1951(95)00109-3.

Roperch, P., G. Herail, and M. Fornari (1999), Magnetostratigraphy of the Miocene Corque basin, Bolivia: Implications for the geodynamic evolution of the Altiplano during the late tertiary, *J. Geophys. Res.*, *104*, 20,415–20,429, doi:10.1029/1999JB900174.

Roperch, P., M. Fornari, G. Herail, and G. V. Parraguez (2000), Tectonic rotations within the Bolivian Altiplano: Implications for the geodynamic evolution of the central Andes during the late tertiary, *J. Geophys. Res.*, *105*, 795–820, doi:10.1029/1999JB900311.

Rosenau, M. (2004), Tectonics of the southern Andean intra-arc zone (38°–42°S), Ph.D. thesis, Freie Univ., Berlin.

Rousse, S., S. Gilder, D. Farber, B. McNulty, P. Patriat, V. Torres, and T. Sempere (2003), Paleomagnetic tracking of mountain building in the Peruvian Andes since 10 ma, *Tectonics*, *22*(5), 1048, doi:10.1029/2003TC001508.

Rousse, S., S. Gilder, M. Fornari, and T. Sempere (2005), Insight into the neogene tectonic history of the northern Bolivian orocline from new paleomagnetic and geochronologic data, *Tectonics*, *24*, TC6007, doi:10.1029/2004TC001760.

Royden, L., and L. Husson (2006), Trench motion, slab geometry and viscous stresses in subduction systems, *Geophys. J. Int.*, *167*, 881–905, doi:10.1111/j.1365-246X.2006.03079.x.

Russo, R. M., and P. G. Silver (1994), Trench-parallel flow beneath the Nazca Plate from seismic anisotropy, *Science*, *263*, 1105–1111, doi:10.1126/science.263.5150.1105.

Russo, R. M., and P. G. Silver (1996), Cordillera formation, mantle dynamics, and the Wilson cycle, *Geology*, *24*, 511–514, doi:10.1130/0091-7613(1996)024<0511:CFMDAT>2.3.CO;2.

Schellart, W. P., J. Freeman, D. R. Stegman, L. Moresi, and D. May (2007), Evolution and diversity of subduction zones controlled by slab width, *Nature*, *446*, 308–311, doi:10.1038/nature05615.

Scheuber, E., K. Hammerschmidt, and H. Friedrichsen (1995), ^{40}Ar/^{39}Ar and Rb-Sr analyses from ductile shear zones from the Atacama Fault Zone, northern Chile: The age of deformation, *Tectonophysics*, *250*, 61–87, doi:10.1016/0040-1951(95)00044-8.

Schmidt, S., and H.-J. Götze (2006), Bouguer and isostatic maps of the central Andes, in *The Andes: Active Subduction Orogeny, Frontiers Earth Sci.*, vol. XXII, edited by O. Oncken et al., pp. 125–146, Springer, Berlin.

Scholz, C., and J. Campos (1995), On the mechanism of seismic decoupling and back arc spreading at subduction zones, *J. Geophys. Res.*, *100*, 22,103–22,115, doi:10.1029/95JB01869.

Sempere, T., et al. (2002), Lithosphere-scale transcurrent fault systems in Andean Southern Peru, paper presented at V International Symposium on Andean Geodynamics, IRD, Toulouse, France, 16–18 September.

Shemenda, A. (1993), Subduction of the lithosphere and back-arc dynamics: Insights from physical modeling, *J. Geophys. Res.*, *98*, 16,167–16,185, doi:10.1029/93JB01094.

Shemenda, A. I. (1994), *Subduction: Insights From Physical Modelling*, 207 pp., Kluwer Acad., Dordrecht, Netherlands.

Sobolev, S., and A. Babeyko (2005), What drives orogeny in the Andes?, *Geology*, *33*, 617–620, doi:10.1130/G21557.1.

Sobolev, S., A. Babeyko, I. Koulakov, and O. Oncken (2006), Mechanism of the Andean orogeny: Insight from numerical modeling, in *The Andes: Active Subduction Orogeny, Frontiers Earth Sci.*, vol. XXII, edited by O. Oncken et al., pp. 513–536, Springer, Berlin.

Song, T.-R., and M. Simons (2003), Large trench-parallel gravity variations predict seismogenic behavior in subduction zones, *Science*, *301*, doi:10.1126/science.1085557.

Tang, J.-C., and A. Chemenda (2000), Numerical modelling of arc-continent collision: Application to Taiwan, *Tectonophysics*, *325*, 23–42, doi:10.1016/S0040-1951(00)00129-3.

Tang, J.-C., A. Chemenda, J. Chéry, S. Lallemand, and R. Hassani (2002), Compressional subduction regime and initial arc-continent collision: Numerical modeling, *Geol. Soc. Am. Spec. Pap.*, *358*, 177–186.

Tichelaar, B., and L. Ruff (1993), Depth of seismic coupling along subduction zones, *J. Geophys. Res.*, *98*, 2017–2037, doi:10.1029/92JB02045.

Uyeda, S., and H. Kanamori (1979), Back-arc opening and the mode of subduction, *J. Geophys. Res.*, *84*, 1049–1062, doi:10.1029/JB084iB03p01049.

Yanez, G. A., C. R. Ranero, R. von Huene, and J. Diaz (2001), Magnetic anomaly interpretation across the southern central Andes (32°–34° S): The role of the Juan Fernandez Ridge in the late Tertiary evolution of the margin, *J. Geophys. Res.*, *106*, 6325–6345, doi:10.1029/2000JB900337.

Zoback, M. L. (1992), First- and second-order patterns of stress in the lithosphere: The world stress map project, *J. Geophys. Res.*, *97*, 11,703–11,728, doi:10.1029/92JB00132.

Zoback, M. L., et al. (1989), Global patterns of intraplate stress: A status report on the world stress map project of the International Lithosphere Program, *Nature*, *341*, 291–298, doi:10.1038/341291a0.

D. A. Boutelier, Helmholtz-Zentrum Potsdam Deutsches GeoForschungsZentrum, telegrafenberg C223, D-14473, Potsdam, Germany. (david@gfz-potsdam.de)

O. Oncken, Helmholtz-Zentrum Potsdam Deutsches GeoForschungsZentrum, telegrafenberg C221, D-14473, Potsdam, Germany. (oncken@gfz-potsdam.de)